Polymer Nanomaterials Hot Paper

How to cite: *Angew. Chem. Int. Ed.* **2022,** *61,* e202208084
International Edition: doi.org/10.1002/anie.202208084
German Edition: doi.org/10.1002/ange.202208084

Regioselective Seeded Polymerization in Block Copolymer Nanoparticles: Post-Assembly Control of Colloidal Features

*Lucila Navarro, Andreas F. Thünemann, Tadahiro Yokosawa, Erdmann Spiecker, and Daniel Klinger**

Abstract: Post-assembly modifications are efficient tools to adjust colloidal features of block copolymer (BCP) particles. However, existing methods often address particle shape, morphology, and chemical functionality individually. For simultaneous control, we transferred the concept of seeded polymerization to phase separated BCP particles. Key to our approach is the regioselective polymerization of (functional) monomers inside specific BCP domains. This was demonstrated in striped PS-*b*-P2VP ellipsoids. Here, polymerization of styrene preferably occurs in PS domains and increases PS lamellar thickness up to 5-fold. The resulting asymmetric lamellar morphology also changes the particle shape, i.e., increases the aspect ratio. Using 4-vinylbenzyl azide as comonomer, azides as chemical functionalities can be added selectively to the PS domains. Overall, our simple and versatile method gives access to various multifunctional BCP colloids from a single batch of pre-formed particles.

Introduction

In nature, complex functions of dispersed systems are governed by colloidal shape, morphology, and chemical functionality at once.[1] Mimicking these features with synthetic particles would give access to new building blocks for advanced applications in biology,[2] photonics,[3] and catalysis.[1,4] However, the realization of such multifunctional colloids is challenging, and existing approaches often rather target these different aspects individually.

To address this challenge, evaporation-induced phase separation of block copolymers (BCPs) has evolved as a powerful strategy.[5] Here, macromolecules are spatially arranged in soft colloidal confinements with high accuracy. For a given BCP, particle shape and morphology can be controlled through the interfacial energies between BCP and surrounding medium, the degree of confinement (droplet/particle size), and the evaporation kinetics.[6] Moreover, utilization of BCPs with different packing parameters (varying block ratio), varying overall molecular weights, or number of blocks can expand the accessible particle structures.[7] Alternatively, incorporation, removal, or change of additives during particle preparation enables colloidal structures that can deviate from the pure BCP systems.[8] In this context, different solvents,[9] switchable surfactants,[6g,10] small molecules,[11] homopolymers,[5a,6b,12] and even other BCPs[12b] have been examined. Overall, these strategies give access to a remarkable variety of new shapes and morphologies that define the properties of resulting materials.[3a,c,13] Unfortunately, the particles are still limited in the spatial distribution of chemical functionalities. While this feature could be controlled through introducing respective functional groups in the BCP building blocks, these chemical groups also influence the BCPs' phase separation.[14] As a result, facile and predictable control over particle shape and morphology is hindered. Thus, most investigations focus on BCPs of limited chemical functionality for the sake of a well-described phase separation behavior. Even though few approaches already use functional BCPs[12a] or blends with functionalized homopolymers,[15] they often require laborious optimization of the phase separation conditions for each new particle composition.

Alternatively, post-assembly modifications can avoid the complex self-assembly of functional BCPs. In such approaches, selected colloidal features can be adjusted after the particle preparation. Mainly (vapor) solvent annealing has been investigated to change shape and morphology of particles through BCP rearrangements after the evaporation of the solvent.[10a,16] Prior to solvent evaporation, the selective swelling of specific polymer segments is also a powerful tool to change the BCP packing parameter and thus transform shape and morphology of (self-assembled) particles.[17] In contrast, the (simultaneous) introduction of chemical functionality after particle preparation is largely

[*] L. Navarro, D. Klinger
Institute of Pharmacy, Freie Universität Berlin
Königin-Luise Straße 2–4, 14195 Berlin (Germany)
E-mail: daniel.klinger@fu-berlin.de

A. F. Thünemann
Bundesanstalt für Materialforschung und -prüfung (BAM)
Unter den Eichen 87, 12205 Berlin (Germany)

T. Yokosawa, E. Spiecker
Institute of Micro- and Nanostructure Research (IMN) & Center for Nanoanalysis and Electron Microscopy (CENEM), Friedrich-Alexander-Universität Erlangen-Nürnberg, IZNF
Cauerstraße 3, 91058 Erlangen (Germany)

unexplored and only few examples on crosslinking[11b] or surface functionalization[14c,18] have been reported. Consequently, a new synthetic post-assembly method is required that would allow the simultaneous modification of particle shape, morphology, and chemical functionality. Such a platform should be versatile, efficient, and synthetically simple, i.e., accessible by non-experts in the field. This would expand the synthetic toolbox that is needed to bring such colloids from fundamental investigations to actual material applications.

In addressing this need, we have developed a new strategy that is based on regioselective seeded polymerization in phase separated BCP particles (Figure 1a). Key to structural control is a three-step process: In the first step, one specific BCP domain is preferably swollen with a functional monomer. In the second step, regioselective polymerization preferably occurs in these domains. Finally, the newly introduced functional groups can be used for spatially controlled modifications. With this process, we aim to translate seeded polymerizations from homogeneous spheres[19] and Janus particles[20] to BCP particles with complex morphologies. Such a strategy has not yet been realized and comprises new challenges and unique opportunities to expand the synthetic toolbox for tuning colloidal properties: We suggest that the spatially controlled polymerization can induce changes in the overall particle structure and functionality.

To determine the potential of this approach, we focused on striped PS-*b*-P2VP ellipsoids as seed particles and styrene as PS-selective monomer (due to its structural resemblance to the PS-preferable solvent toluene).[19a,21] In such stacked lamellar structures, we assume that preferable seeding of the PS domains has limited effects on the P2VP lamellae. We hypothesize that the final structure consists of asymmetric lamellae, i.e., different BCP domains with different thicknesses (see Figure 1a). Since we suggest that this feature can

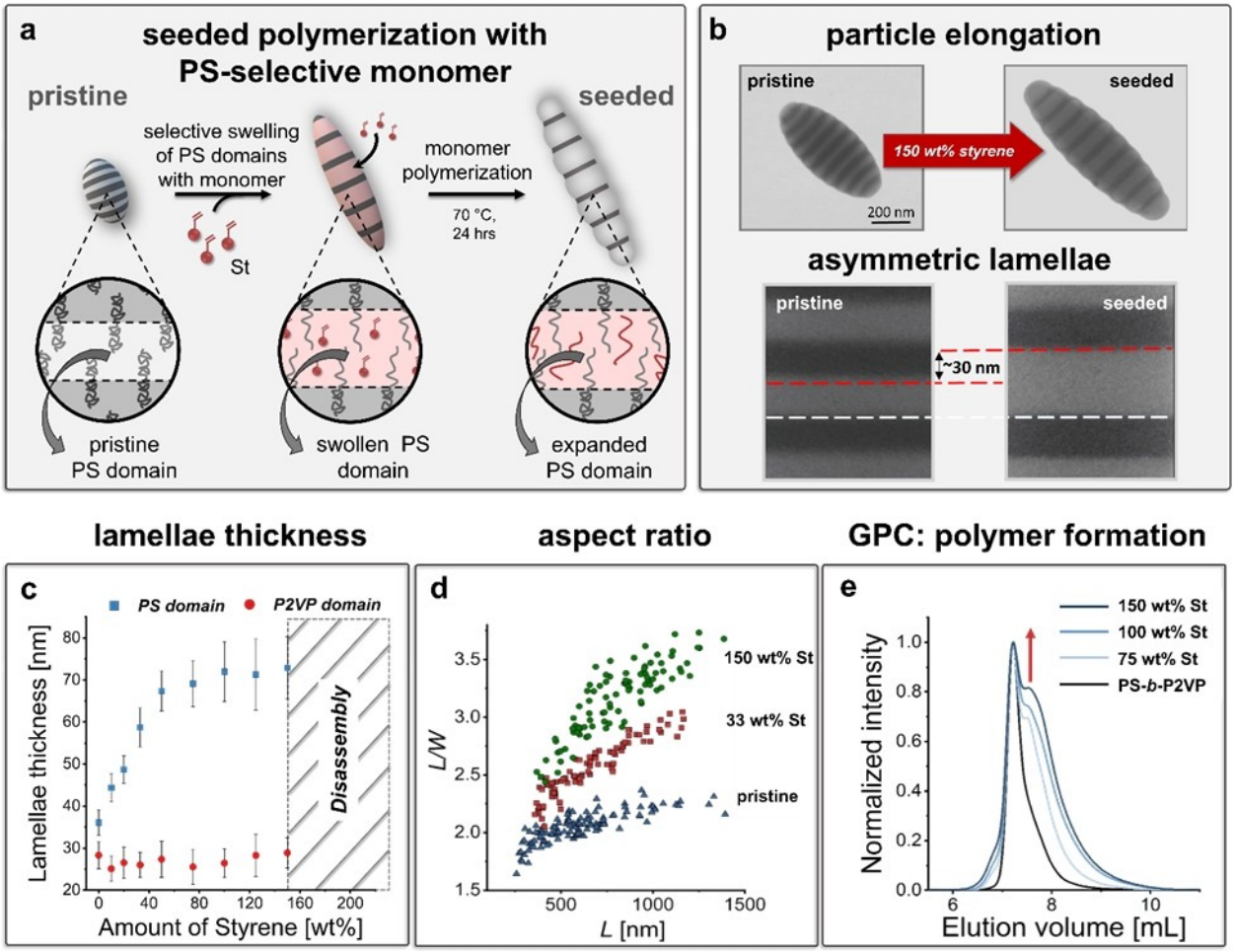

Figure 1. Seeded polymerization of styrene in PS-*b*-P2VP particles enables control over particle morphology and shape. a) Schematic representation of the seeded polymerization process: Starting from striped ellipsoidal particles, PS domains are preferably swollen with St (and AIBN). Polymerization expands the PS lamella, which translates to an asymmetric lamellae morphology and particle elongation. b) TEM images of particles before and after the seeded polymerization with 150 wt% St show a pronounced increase in PS lamellae thickness and particle elongation. c) Thickness of PS domains gradually increases with the amount of styrene during the seeded polymerization. In contrast, the P2VP lamellae remain unchanged. d) Dependency of particle aspect ratio on the amount of styrene. As in the pristine particles, larger particles show higher aspect ratios. e) GPC of seeded particles shows the successful formation of *h*PS homopolymers during the seeded polymerization.

be controlled by the amount of styrene, the seeding process avoids the challenging phase separation of complex miktoarm star copolymers that are otherwise required for such asymmetric lamellae.[22] In addition, we suggest that the anticipated increase in PS domain size also translates to the z-axis of the particles (perpendicular to the lamellae) which induces a particle elongation. Thus, this strategy would represent a facile and robust alternative to tailor lamellar thickness and aspect ratio of such colloidal ellipsoids. In addition, using 4-vinylbenzyl azide (VBA) as reactive monomer, is assumed to allow further domain-specific functionalization through azide-alkyne "click" chemistry.[23] Overall, the simplicity and versatility of this new method provides a new tool for precise control of particle shape, internal anisotropy, and domain-selective functionalization.

Results and Discussion

Seeded Polymerization of Styrene in PS-*b*-P2VP Particles

To demonstrate selective BCP domain expansion, we examined the seeded polymerization of styrene (St) in striped ellipsoidal PS-*b*-P2VP ($M_{n,Ps}=102$ kDa, $M_{n,P2VP}=97$ kDa) particles. For this, the pristine (non-seeded) particles were prepared by our previously reported method that uses a mixed-surfactant system to provide a neutral BCP/water interphase.[6c] After particle preparation, different amounts of styrene (St), containing a dissolved radical initiator (AIBN), were added to a degassed particle dispersion via micropipette. In contrast to vapor annealing processes, this direct addition circumvents the uncontrolled transfer of the monomer from a vapor phase to the dispersion. As a result, the styrene amount can be controlled precisely between 10 and 250 wt % with respect to the total mass of pristine particles. Following styrene addition, the particles were briefly sonicated to facilitate diffusion of the monomer into the particles. After a predetermined swelling time to ensure complete styrene uptake, the polymerization was induced by heating. To stop the seeded polymerization, the reaction was opened to air and any unreacted styrene monomer was evaporated at room temperature.

After the seeded polymerization, particle shapes and morphologies were examined via transmission electron microscopy (TEM). Image analysis revealed a selective increase of PS domain size with the amount of added styrene (c_{St}) (Figure 1). For 150 wt % of St, this effect becomes most prominent, and the PS lamellae thickness (d_{PS}) increased from 38 ± 3 nm (before seeded polymerization) to 73 ± 7 nm (after seeded polymerization) (Figure 1b). By using intermediate amounts of styrene, d_{PS} can be tuned precisely (Supporting Information, Figure S1 and S2). The corresponding increase of d_{PS} follows a two-stage profile as shown in Figure 1c. First, varying c_{St} from 10–50 wt % causes a steep increase in PS domain size to ca. 70 nm. Second, the addition of more styrene up to 150 wt % only increases d_{PS} very slowly. We assume that this profile stems from changing contributions of: i) stretching of the BCP's PS chains and ii) added mass by the formed PS homopolymer (*h*PS). At low c_{St}, we suggest that both factors contribute. This means stretching of the BCP's PS chains has a big impact on the expansion of the PS domains. However, upon exceeding 50–70 mol % of styrene, we assume that the influence of the PS stretching becomes negligible, i.e., the segments are almost fully stretched. Thus, any further increase in d_{PS} mostly stems from the introduced mass of *h*PS. In contrast to this expansion of PS domains, the thickness of the P2VP domains (d_{P2VP}) remains similar to the pristine particles over the whole range of styrene contents (10–150 wt %) (Figure 1c). This selective expansion of the PS domains creates an asymmetric lamellar morphology with PS lamellae being thicker than P2VP lamellae. Since the width of both domains is not affected, the lamellar asymmetry is accompanied by particle elongation (see Figure 1b). In other words, the morphological change directly translates to a transformation in the overall particle shape. This can be quantified by the particles' aspect ratio ($AR=L/W$). As shown in Figure 1d and Figure S3 (Supporting Information), AR clearly increases with the amount of styrene. In addition, AR also increases with the overall particle size (defined by the particle length (L)). This second effect stems from the preparation of the pristine particles. Here, during BCP phase separation, larger particles are easier to deform into ellipsoids due to smaller surface energy contributions. Thus, AR differences after the post-assembly modification are predetermined by the differences in the pristine particles. As a result, AR still increases with L for all samples after the seeded polymerization (Figure 1d and Figure S3). Combining both effects, AR can almost double upon the seeded polymerization with 150 wt % St in large particles ($L>750$ nm).

It becomes obvious that our synthetic strategy enables accurate control over particle morphology and shape. To expand this strategy to the incorporation of chemical functionality, it needs to be ensured that potential functional monomers are immobilized via actual polymerization in the specific domains. Thus, the observed structural changes need to be assigned to monomer polymerization inside the particles and not to potential BCP rearrangement effects. Such alternative effects could be caused by a reversible swelling or annealing of the polymer chains with styrene as preferred solvent for the PS domains.[24] To distinguish these two processes, the following control experiments were performed:

First, we confirmed the formation of PS homopolymers (*h*PS) inside the particles via gel permeation chromatography (GPC). For this, we examined the molecular weight of the particles' polymer building blocks after the seeded polymerization. Figure 1e shows the GPC elution volume profile for dissolved pristine particles and for particles seeded with 75, 100 and 150 wt % of St. In all seeded samples, a new peak with $M_n=90$ kDa was observed at elution volumes higher than the initial BCP ($V_{el.,max}=7.2$ mL, $M_{n,PS\text{-}b\text{-}P2VP}=199$ kDa). This new peak increases in intensity with the amount of styrene during the seeded polymerization, thus suggesting the formation of *h*PS.

Next, we demonstrated that such asymmetric lamellae structures can only be realized through polymerization after particle assembly. For this, we performed control experiments where we added a *h*PS homopolymer already during the initial particle preparation. In this case, we used blends of PS-*b*-P2VP and *h*PS ($M_n = 90$ kDa) to mimic the composition of particles after the seeded polymerization with 150 wt % styrene (Supporting Information, Figure S4a). After the solvent evaporation-induced phase separation, the resulting particles do not exhibit a defined lamellae morphology or an ellipsoidal shape. Instead, ill-defined structures were observed (Supporting Information, Figure S4b). Such a disturbance of the lamellar morphology upon BCP phase separation is a well-known result of a changed volume ratio between blocks upon the addition of homopolymers.[6b,12d,25] Here, the addition of *h*PS increases the PS volume fraction in the PS-*b*-P2VP system. While such homopolymer/BCP blending strategies can be used to adjust the morphology of BCP particles during their preparation, accurate control over additional parameters, e.g., homopolymer molecular weight, blending ratio etc., is needed to obtain defined morphologies.[12f] In contrast, our post-assembly modification approach can circumvent the corresponding optimizations and access new morphologies. Overall, these experiments highlight the necessity of introducing *h*PS after the initial BCP phase separation if an asymmetric lamellar morphology should be obtained.

Ultimately, the seeded polymerization was directly compared to the influence of the above-mentioned potential solvent annealing effect.[16h] Here, we have recently demonstrated that toluene can induce morphological changes in striped ellipsoidal PS-*b*-P2VP particles. We suggest that preferable swelling of PS domains is accompanied by a less pronounced swelling of P2VP domains i.e., plasticization. The combination of both effects induces pronounced stretching of PS chains and partial migration of P2VP segments to the particle/water interphase. Resulting enthalpic contributions can stabilize the morphological transition after toluene removal.[24] Comparing this annealing process to our seeded polymerization method, we assume that non-polymerized styrene can behave similar to toluene, i.e., as preferable solvent for PS in PS-*b*-P2VP materials.[21d–f] Thus, we aimed to examine whether non-polymerized styrene can induce a comparable morphological change. For this, we performed control experiments by adding styrene but not the radical initiator (AIBN).

After heating and evaporation of unreacted styrene, a selective expansion of the PS domains was observed to be similar as in the toluene annealed samples. More importantly, the morphological transition was also similar to the changes observed during the seeded polymerization process (Supporting Information, Figure S5). However, in case of a purely annealing based transition, the physical expansion of the PS domains is fully reversible upon a second annealing steps with chloroform as a good non-selective solvent.[24] Similarly, for the styrene-swollen control samples, we also observed a complete reversal to the pristine morphology after annealing with chloroform as good solvent for both blocks (see Supporting Information, Figure S6). In direct contrast, the particles that underwent the seeded polymerization process (styrene + AIBN), did not show structural reversibility upon subsequent annealing with chloroform. Instead, these particles showed a morphological transition to non-lamellar structures resembling the phase separation of PS-*b*-P2VP/*h*PS blends (see Supporting Information, Figure S6). Thus, these experiments further support the suggested formation of *h*PS during the seeded polymerization step.

While these experiments demonstrate the successful polymerization of styrene inside phase separated particles, the adjustment of particle shape and lamellae asymmetry is restricted to the range of 10–150 wt % of styrene. Further increasing c_{St} leads to increasing particle fragmentation, i.e., the breakage into smaller particles (Figure 1c, Figure 2, Figure S7). Starting at 150 wt % of St, we can already observe spherical P2VP-covered PS particles that are detached from the striped ellipsoids. Further increasing c_{St} to 175 and 200 wt % leads to detachment of P2VP-covered PS spheres with multiple P2VP cores. Finally, 250 wt % of St induces a complete restructuring of the ellipsoids to spherical particles with multiple P2VP cores.

Regarding the destabilization mechanism, we assume that styrene does not only swell the PS domains but can also plasticize the P2VP domains. The resulting mobility of both domains allows structural rearrangements to minimize the energy of the system, i.e., through increasing the energetically favored interface between P2VP and water.[11b] At the tips of the particles, this leads to disruption of the P2VP lamellae which is accompanied by fusion and separation of the last PS lamellae. Together, this generates (P2VP containing) PS spheres covered with a thin P2VP layer. In general, a potential segregation of *h*Ps in the PS domains could induce physical stress that enhances the observed delamination. However, we observed very similar particle disintegration in our previous study where particles were annealed/swollen with toluene ($c_{tol} > 200$ wt %) and did not undergo the polymerization step.[24] Thus, we assume that particle fragmentation mainly occurs during the swelling stage of our process.

Overall, these results suggest that P2VP plasticization has a profound influence on the overall process. Thus, our suggested mechanism for the seeded polymerization also needs to consider the following scenario: While styrene preferably swells the PS domains, the amount of styrene in the P2VP domains is not negligible. Thus, polymerizations could also start in these locations. In this case, we assume that growing *h*PS oligomers will become increasingly incompatible with the P2VP domains and migrate into the PS domains where polymerization continues. Consequently, we assume that the majority of the polymerization still occurs regioselectively in the PS domains. However, the mobility of the P2VP segments still limits the accessible lamellar asymmetry and particle elongation during the seeded polymerization. Thus, utilization of high monomer contents (> 150 wt %) requires stabilization of the P2VP lamellae to prevent particle disintegration.

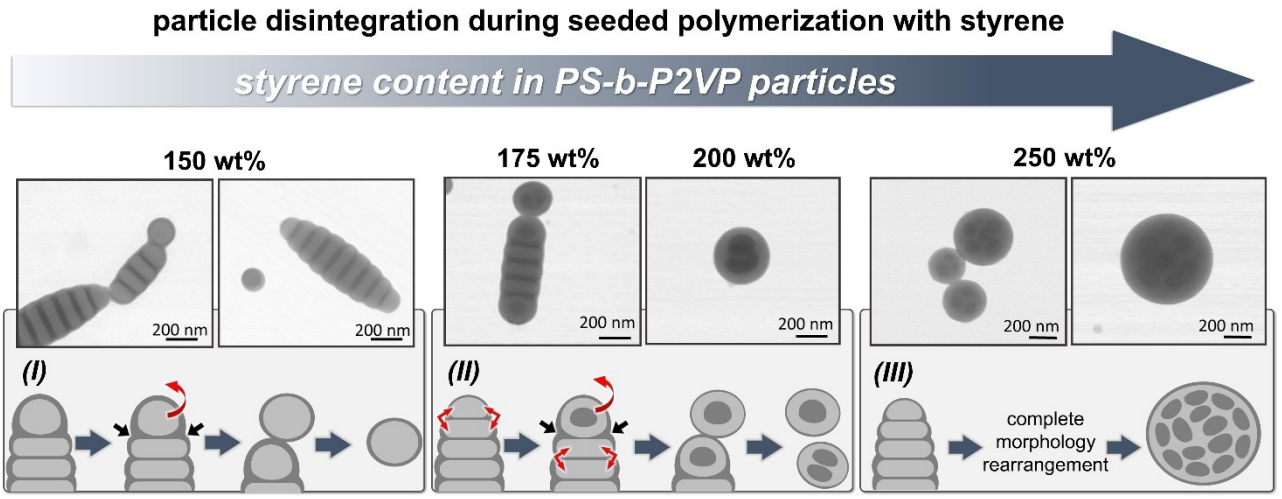

Figure 2. Particle fragmentation during seeded polymerization depends on the amount of styrene (c_{St}). Three different stages where observed: (I) For $c_{St} \approx 150$ wt%, detachment of single PS domains from the particle tips gives spherical PS particles that contain a thin P2VP shell. (II) Upon increasing c_{St} to 175 wt% and 200 wt%, multiple lamellae detach from the particles. This generates spherical PS particles with (multiple) P2VP cores and a P2VP shell. (III) For $c_{St} \geq 250$ wt%, a complete rearrangement of the particles to spheres with multiple internal P2VP domains is observed.

*Seeded Polymerization of Styrene in PS-b-*P2VP Particles with Crosslinked P2VP Domains

Structural stabilization of the P2VP domains was achieved by crosslinking with 1,4-dibromobutane (DBB) through pyridinium quaternization. Since this process is not quantitative in dispersion, excess amounts of DBB were added: 50 mol% and 100 mol% with respect to the 2VP groups (Supporting Information, Figure S8). As demonstrated by Kim and co-workers, these amounts can already induce a morphological change in the particles.[11b] In our case, for both DBB contents, the PS lamella thickness increases from 38 nm (pristine particles) to ca. 60 nm while the P2VP lamellae thickness slightly decreases from 29 nm (pristine) to ca. 25 nm (crosslinked) (Supporting Information, Figure S8b). To confirm the intended structural stabilization of the particles, the dispersions were acidified to pH ≈ 2. At this pH, protonation and solubilization of non-crosslinked P2VP domains would induce a particle disintegration into PS discs.[6c,7c] However, TEM analysis revealed that both crosslinking degrees are sufficient to avoid particle fragmentation (Supporting Information, Figure S8c and Figure S8d).

The stabilized particles were then subjected to the seeded polymerization process with increasing amounts of styrene (Supporting Information, Figure S9 and Figure S10). For particles crosslinked with 50 mol% DBB, the lamellar structure was stable until the utilization of 300 wt% St (Supporting Information, Figure S9a). Thus, successful P2VP stabilization enabled seeded polymerizations with higher c_{St} as for the non-crosslinked particles. However, exceeding this critical amount, particles started to break into conic-like structures. Interestingly, fragmentation occurs through the PS domains rather than through the P2VP domains as in the non-crosslinked particles (Supporting Information, Figure S9b and Figure S9c). Consequently, this mechanistic difference demonstrates stabilization of the P2VP lamellae.

For particles with an increased crosslinker amount of 100 mol% DBB, no particle breakage was observed for even higher styrene contents up to 500 wt% (Figure 3). In this case, a maximum increment of $\Delta d_{PS} = 147$ nm was obtained. Thus, the PS domain thickness increases almost by a factor of 5 without particle disintegration. Hence, P2VP crosslinking can successfully stabilize the expanding PS domains.

Examining this stabilization effect in more detail, we had a closer look on the crosslinked particles before the seeding procedure. Here, TEM images showed a partial migration of P2VP segments to the particle/water interphase.[24] Due to the preferential interaction of quaternized P2VP with water, the particles are covered with a thin P2VP mesh. We assume that the crosslinking density of this surface layer determines the structural stability of the lamellar structure as follows: Upon seeded polymerization, the expansion of the PS domains stretches this surrounding crosslinked P2VP network. In case of particles crosslinked with 50 mol% DBB, the stability of this mesh is not sufficient to prevent particle fragmentation through the PS domains, i.e., the mesh breaks. In contrast, for particles with 100 mol% DBB, the mesh at the surface stretches and stabilizes the expanding PS domains.

The successful structural stabilization allows varying the lamellae thickness over a broad range by the seeded polymerization (see Figure 3a–d, Supporting Information Figure S11). Statistical evaluation (from TEM) shows a gradual growth of the PS lamellae with increasing amounts of styrene: d_{PS} increases from 38 ± 4 nm (pristine) to 185 ± 10 nm (400 wt% St). Higher monomer contents increase the PS lamellae thickness only marginally. We suggest that this can be attributed to the non-linear geometrical

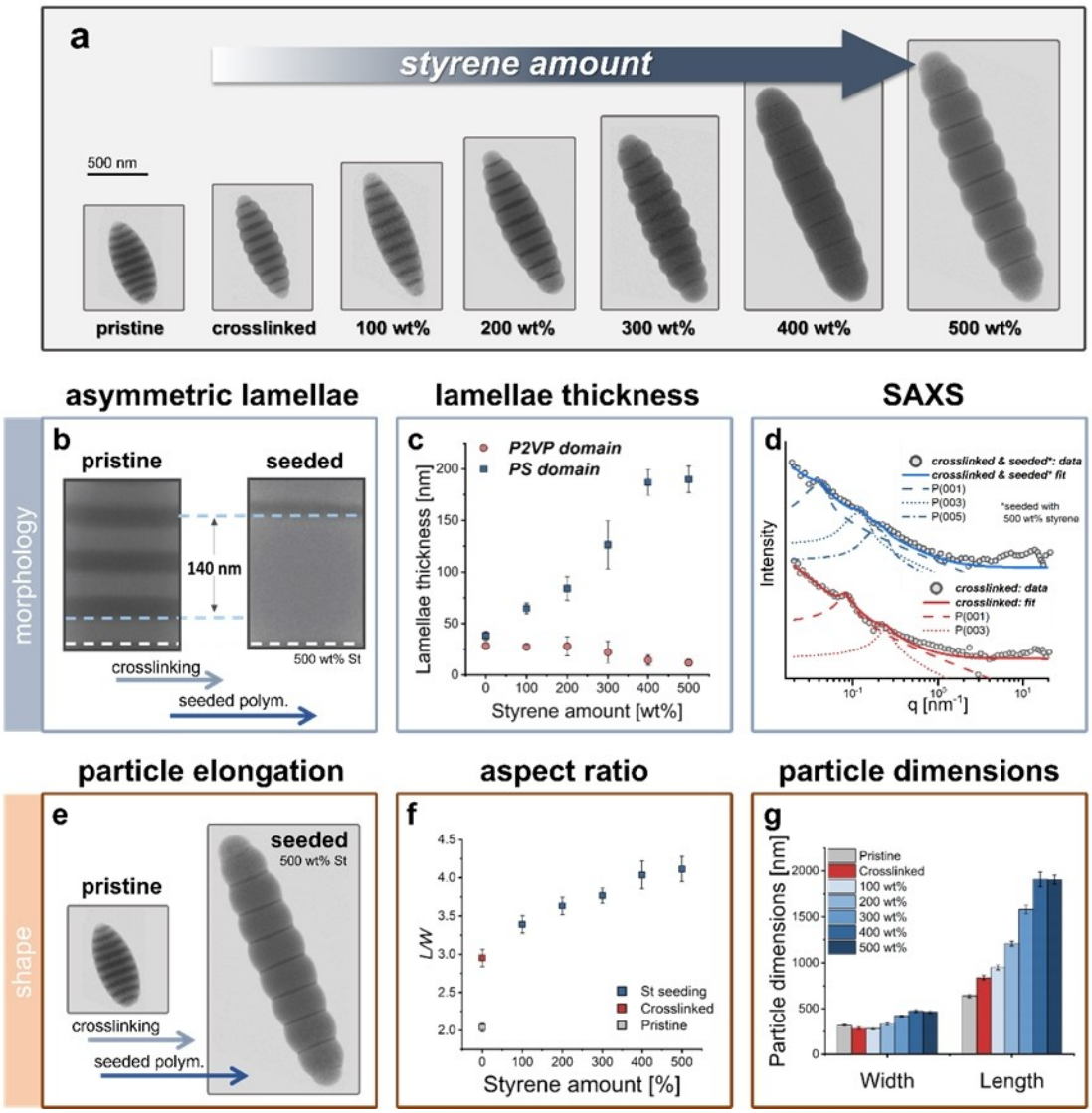

Figure 3. Pronounced structural changes are possible by covalent stabilization of the PS-*b*-P2VP ellipsoids (P2VP crosslinking with 100 mol% DBB). a) Direct comparison of particles with 10 PS lamellae demonstrates the evolution of colloidal features upon increasing c_{St}. PS lamellae thickness and particle elongation increase significantly with styrene content. b) For 500 wt% of styrene, d_{PS} increases about 140 nm, thus leading to a highly asymmetric lamellae morphology. c) The average PS lamellae thickness increases gradually with c_{St}. In contrast, a slight decrease of d_{P2VP} is observed. Depicted values are averages from different particles and different locations in the domains (edge and center). d) SAXS patterns of crosslinked particles (100 mol% DBB) in comparison to crosslinked + seeded particles (200 wt% St) show a shift of domain spacing to larger values. e) For 500 wt% of styrene, particle length (*L*) increases about 3-fold. f) For particles with 10 PS lamellae, *AR* increases gradually with c_{St} and almost doubles for 500 wt% of styrene. g) Particle dimensions of seeded particles (10 PS lamellae) show a significant increase in particle length (*L*). For $c_{St} \geq 200$ wt%, also the particle width (*W*) increases.

relation between volume and thickness of the lamellae. At higher volumes, a corresponding increase in thickness is less pronounced. In addition, we assume that, at this point, the surrounding crosslinked P2VP layer is maximally stretched, thus preventing further PS expansion. Accompanying the PS extension, we observe a gradual reduction of the P2VP lamellae thickness. Increasing c_{St} leads to a reduction of d_{P2VP} from 29 ± 3 nm (pristine) to 13 ± 3 nm (400 wt% St addition). In this case, we suggest that the crosslinked P2VP mesh couples the expansion in z-direction to a stretching in the *x*,*y*-direction (particle short axis).

Overall, both factors (d_{PS} increase and d_{P2VP} decrease) contribute to an increasing domain spacing $d = d_{PS} + d_{P2VP}$ upon seeded polymerization. This can be confirmed by small angle x-ray scattering (SAXS). To demonstrate this effect, we examined crosslinked particles in comparison to samples that were subjected to a subsequent seeded polymerization with 200 wt% and 500 wt% styrene (Figure 3d and Supporting Information Figure S12). For crosslinked particles, peak maxima are detected at $q_1 = 0.08\ nm^{-1}$ and $q_2 = 0.240\ nm^{-1}$ and can be indexed as (001) and (003) since $q_2 = 3q_1$. These values can be used to calculate the domain spacing (the long period) to $d = 2\pi/q_1 = 79$ nm. For the particles seeded with

$c_{St}=200$ wt %, the SAXS curve displays also the (001) and (003) reflections but the peak maxima are shifted to smaller q-values of 0.049 nm^{-1} and 0.147 nm^{-1}, respectively (Supporting Information, Figure S12). These values correspond to a lager long period of $d=130$ nm, i.e., an increase of 51 nm in comparison to the non-seeded particles. Finally, the SAXS curve of particles seeded with $c_{St}=500$ wt % displays (001), (003) and (005) reflections at $q=0.039$ nm^{-1}, 0.117 nm^{-1}, and 0.195 nm^{-1}, corresponding to a long period of 160 nm and an increase of about 81 nm in comparison to the non-seeded particles. The additional reflectance (005) points towards a strong asymmetry in the lamellar structure where one domain is thicker than the other. In addition, we determined the correlation length (l_c) in all samples from the width of the (001) reflections. The obtained values are $l_c=630$ nm, 790 nm and 790 nm for $c_{St}=0$ wt %, 200 wt % and 500 wt %, respectively. These values are comparable to the overall length of the particles and indicate a very regular alignment of the lamella in normal direction to the lamellar plane. The large values of the correlation lengths and the increase in domain spacing for each styrene addition (+ 51 nm and +81 nm, respectively) support the trend observed via TEM.

The increasing domain spacing also translates to particle elongation during seeded polymerization (Supporting Information, Figure S10). However, a quantitative correlation between AR and c_{St} is challenging because elongation also depends on particle length (L) and therefore the corresponding number of lamellae per particle (see Supporting Information, Figure S13).[6c,24] Thus, accurate evaluation of the elongation effect requires comparison of particles with the same number of lamellae (Figure 3a). For particles with 10 PS lamellae each, a clear trend is observed, and the aspect ratio gradually increases with c_{St} (Figure 3f). For the highest amount of styrene, AR doubles from 2.1 ± 0.1 ($c_{St}=0$ wt %) to 4.1 ± 0.2 ($c_{St}=500$ wt %).

While this change in particle shape is significant, a 2-fold increase in AR does not match the observed 4.8-fold increase in PS domain thickness (from 38 nm to 185 nm for $c_{St}=500$ wt %, see Figure 3b, c). This discrepancy can be explained by an associated increase in particle width for styrene contents above 200 wt % (Figure 3g). Up to this amount, the particle width remains constant and AR increases exclusively due to the longitudinal stretch of the PS lamella. However, higher amounts of monomer ($c_{St}>200$ wt %) induce a concurrent particle expansion in length and width. As a result, the styrene-dependent increase in $AR=L/W$ does not exhibit the same exponential trend as the increasing PS domain thickness (Figure 3c and Figure 3g). This effect is emphasized by a concomitant reduction in the P2VP lamellae thickness.

Consequently, the changes in particle shape are not based on PS expansion alone, but rather indicate complex morphological transitions.

Based on TEM image analysis, we suggest the following pathway for particle transformation upon crosslinking and increasing c_{St} (Figure 4): In the first stage, crosslinking of the P2VP domains induces partial P2VP migration to the particle surface. In the second stage, the seeded polymerization of styrene increases d_{PS} without changing the P2VP lamellae. Only the crosslinked P2VP mesh at the surface gets thinner as it stretches. This is observed for styrene contents up to 100 wt %. For $c_{St}\geq200$ wt %, a third stage can be identified where the overall lamellar structure changes. Here, the seeded polymerization induces a transition from flat PS/P2VP domains to stacks of concave PS discs and convex P2VP discs (Figure 4a, b). At $c_{St}=300$ wt %, this effect is maximally pronounced as demonstrated by the differences between lamellar thickness at the middle or the edge. In this stage, the particle width (W) does not increase since stretching of the P2VP surface mesh still permits longitudinal PS expansion. In the fourth stage at $c_{St}\geq$ 400 wt %, the PS/P2VP interphase flattens again, dP2VP decreases, and the particle width increases. We assume that, at this stage, the crosslinked P2VP surface mesh is maximally stretched. Thus, further expanding the PS domains creates sufficient force to laterally stretch the P2VP domains in the particles. As a result of these different contributions, the increase in AR ratio reaches a plateau for 400–500 wt % of styrene.

Incorporation of Functional Monomers through Seeded Polymerization

Combining this structural control with additional chemical functionality would enhance the versatility of our approach significantly. To realize this multifunctionality, we suggest the utilization of functional/reactive monomers during the seeded polymerization (see Figure 5a). In this process, a potential monomer should provide the following features: First, it should contain a reactive group that is compatible with the radical polymerization thus enabling subsequent particle functionalization. Second, a structural similarity between monomer and BCP repeat units should ensure successful incorporation into the particles through swelling and polymerization.

Based on these considerations, we used 4-vinylbenzyl azide (VBA). In this monomer, the reactive azide group enables fast and quantitative CuAAC click functionalization while the styrene-based structure favors seeded polymerization inside the particles. However, the actual location of the polymerization in the phase separated BCP needs to be adjusted to retain control over particle morphology and shape. To control the internal distribution of PVBA, we aim to adjust the polymer's compatibility with the specific PS or P2VP domains. For this, we suggest the formation of random copolymers with a respective second monomer.[15] For example, to favor incorporation of PVBA into the PS domains, we suggest the formation of PVBA-*co*-PS copolymers. To test this hypothesis, we performed a series of seeded polymerizations with different ratios of $c_{VBA}:c_{St}$ (for a constant overall monomer content of $c_{VBA}+c_{St}=400$ wt %). As demonstrated by the azide bands in FTIR spectroscopy, VBA was successfully included into all particles and its incorporation increased with c_{VBA} (see Supporting Information, Figure S14, S15).

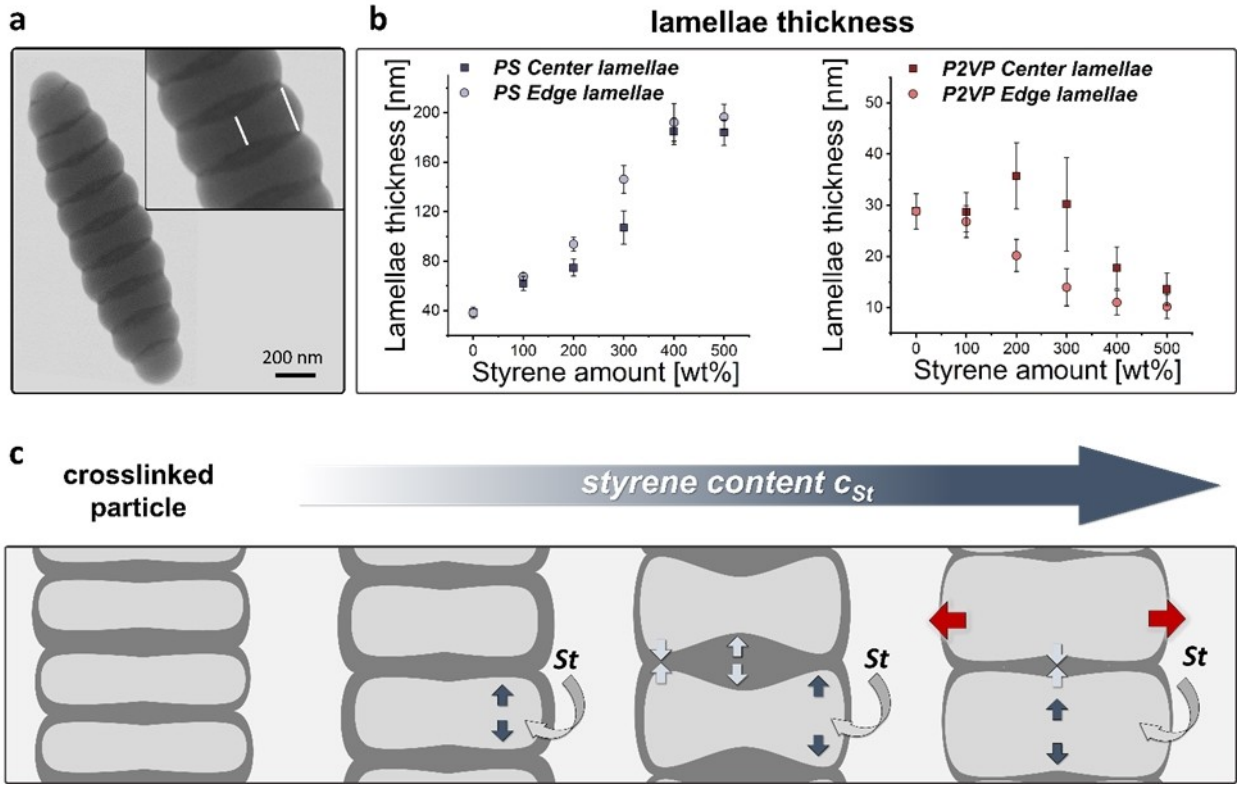

Figure 4. Influence of styrene content on the lamellar morphology of crosslinked seeded particles. a) For styrene contents between 200–300 wt%, the flat lamellae transform into stacks of concave PS discs and convex P2VP lamellae. b) Differences between lamellae thickness at the edge and the middle of the particles can be used to quantify the lamellar transformation. c) Schematic representation of the proposed transformation pathway that is based on PS expansion and stretching of the crosslinked P2VP segments.

Regarding the particle morphology, TEM analysis revealed a structural evolution upon increasing the $c_{VBA}:c_{St}$ ratio (see Figure 5b and Figure S15, Supporting Information). It could be demonstrated that ratios of $c_{VBA}:c_{St}<20:80$ enable the selective incorporation of the copolymers into the PS domains. However, with increasing VBA content, the resulting PVBA-*co*-PS phase separates inside the PS domains. For pure PVBA, a distinct new phase was observed inside the PS domains, thus resulting in particles of complex morphologies with 3 different domains. Such a complex phase separation behavior was also observed in control experiments with methyl methacrylate (MMA) as a structurally dissimilar monomer for both blocks of PS-*b*-P2VP. In this case, the seeded polymerization resulted in a PMMA shell surrounding the striped ellipsoidal PS-*b*-P2VP particles (see Supporting Information, Figure S16). These results emphasize the importance of adjusting polymer compatibility to control the spatial distribution of the new-formed polymer.

Particles with a homogeneous distribution of PVBA-*co*-PS in the PS domain ($c_{VBA}:c_{St}<20:80$) represent a perfect balance between incorporation of functional azide groups and retention of the structural control. To demonstrate the chemical functionality of such reactive particles, two different alkyne-containing moieties were coupled through CuAAC reactions. First, an organic dye (TAMRA) was used to follow the functionalization via UV/Vis spectroscopy (see Supporting Information, Scheme S1). Second, an alkyne-functionalized ferrocene (FCN) was used to demonstrate the spatially-controlled functionalization via TEM (see Supporting Information, Scheme S2).

During the functionalization with TAMRA-alkyne, successful coupling is already visible by eye. Figure 5c and Figure S17a (Supporting Information) show that the dye-coupled particle suspension appears pink, whereas the negative control (added dye but no catalyst) shows a colorless (white) appearance. Since these images are taken after several washing steps to remove any unreacted dye, successful coupling is suggested. Moreover, the functionalization is also visible in the UV/Vis spectra of the particle dispersions. Here, it is observed that the absorbance intensity increases with a higher concentration of alkyne-TAMRA (Figure 5c and Supporting Information, Figure S17b).

The functionalization with FCN can be visualized directly by TEM due to the good Z-contrast of the iron from FCN (see Supporting Information, Figure S18). More detailed investigations are possible through spatially resolved energy-dispersive X-ray spectroscopy based on scanning transmission electron microscopy (STEM-EDX). Figure 5d shows a respective profile of a FCN-functionalized particle. Pink color corresponds to iron (Fe) and blue color to carbon

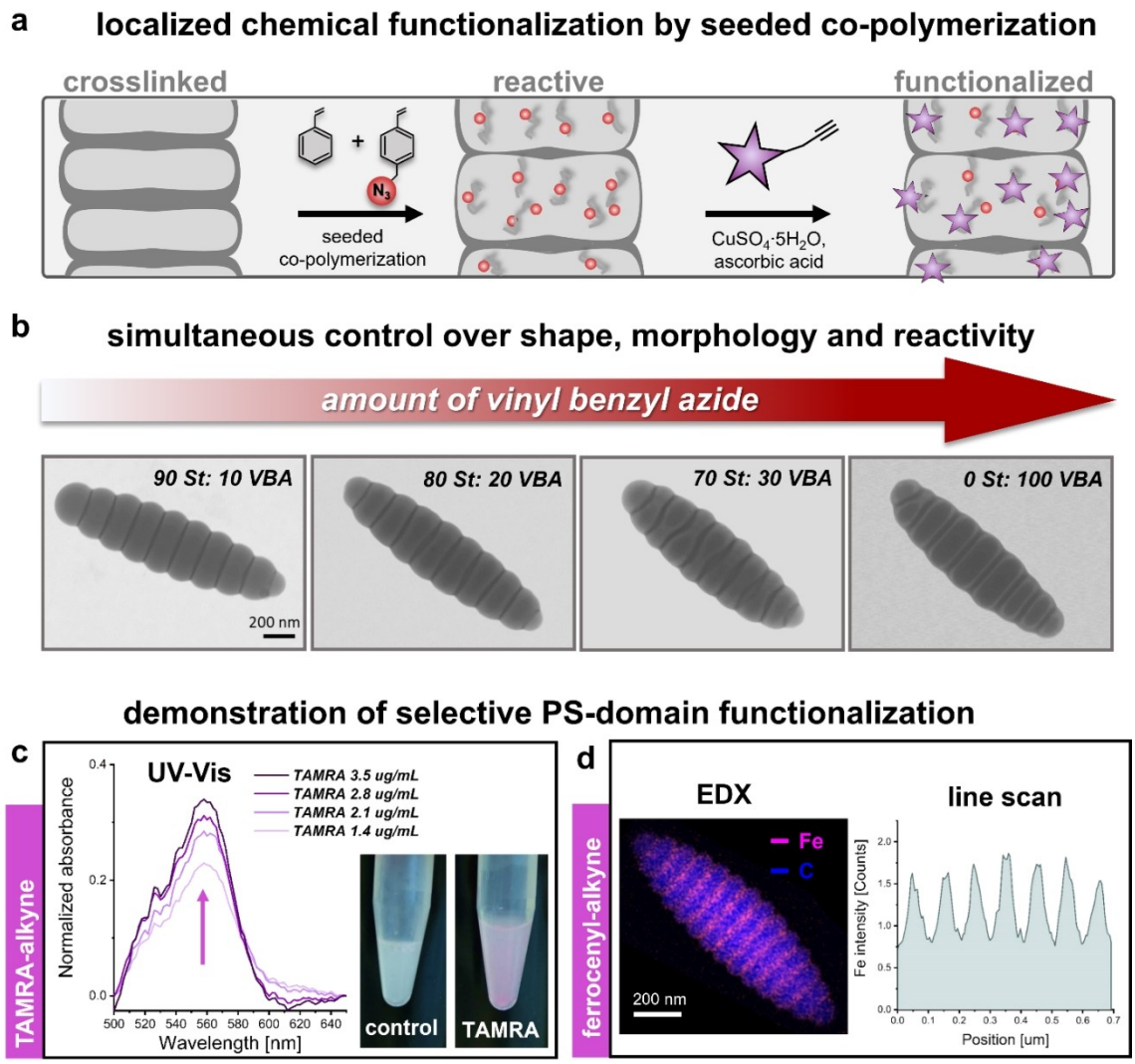

Figure 5. Simultaneous control over particle shape, morphology and chemical functionality via seeded polymerization with 4-vinyl benzyl azide (VBA). a) Schematic representation of the synthetic strategy: Crosslinked PS-*b*-P2VP particles are swollen with mixtures of styrene and VBA. Co-polymerization of both monomers selectively incorporates reactive azide groups in the PS domains. These can be used for click reactions with alkyne-bearing moieties while retaining control over shape and morphology. b) TEM images demonstrate the structural evolution of PS-*b*-P2VP particles after seeded polymerization with different ratios of c_{St}/c_{VBA} (constant total monomer content $c_{St}+c_{VBA}=400$ wt%). c) Particle functionalization with an alkyne-functionalized dye (alkyne-TAMRA) is visible by eye. UV/Vis absorbance of dye-functionalized particles further confirm successful coupling. Spectra depict the signal after deducting the absorbance of control particles (without the catalyst). d) Particle functionalization with an alkyne-functionalized ferrocene (FCN-alkyne) is demonstrated by EDX analysis in TEM. A line scan perpendicular to the lamellae reveals the periodic distribution of Fe, thus suggesting the spatially controlled incorporation of FCN.

(C). It can be seen that Fe location follows the well-defined periodic pattern of PS lamellae. This can be visualized by a line scan perpendicular to the lamellae. Overall, the successful TAMRA and FCN coupling demonstrate the high synthetic potential of the reactive particles.

Conclusion

We have demonstrated a new post-assembly strategy to control the colloidal features of phase separated BCP nanoparticles. Our approach is based on the seeded polymerization of (functional) monomers inside preformed BCP particles. Here, compatibility between monomer and a specific BCP domain determines the location of the seeded polymerization inside the particles. While the corresponding change in domain thickness translates to a particle elongation, the monomer reactivity introduces spatially controlled chemical functionality.

In striped PS-*b*-P2VP ellipsoids, we were able to demonstrate the selective expansion of PS domains by seeded polymerization with styrene. Mechanistical studies revealed that structural stabilization of P2VP domains was required to allow an extremely high d_{PS} increment (up to 5-fold increase). In this case, we observed a distinct asymmetric lamellae morphology with an unprecedented

level of internal anisotropy. Such a structural control can neither be achieved by conventional phase-separation of asymmetric BCPs nor by established post-assembly modifications. In addition, the robustness of this strategy enabled simultaneous particle functionalization. Spatially-controlled copolymerization with VBA allowed PS-selective incorporation of azide functionalities for subsequent CuAAC click functionalization.

In general, we suggest that this strategy can significantly expand the synthetic toolbox for the adjustment of colloidal features in BCP particles. We assume that our approach can be extended to other BCP particles and monomers. For this, the compatibility between BCP segments and monomers needs to be considered carefully. Ultimately, monomers that combine orthogonal domain selectivity and orthogonal reactivity could enable differently functionalized lamellae. This strategy would pave the way to compartmentalizing different (macro-)molecules in dispersed particles. As a result, such new colloidal systems would represent advanced building blocks for potential applications that include: The utilization of anisotropic particle shape and periodic chemical functionality to tailor interactions with biological systems and the domain-selective incorporation of different catalytic systems to examine the influence on cascade reactions.

Acknowledgements

The authors would like to thank Glen J. Smales for help in SAXS measurements. L.N. acknowledges funding from the European Union's Horizon 2020 research and innovation programme under the Marie Skłodowska-Curie grant agreement No [838448]. Furthermore, the authors acknowledge the assistance of the Core Facility BioSupraMol supported by the Deutsche Forschungsgemeinschaft (DFG). Open Access funding enabled and organized by Projekt DEAL.

Conflict of Interest

The authors declare no conflict of interest.

Data Availability Statement

The data that support the findings of this study are available from the corresponding author upon reasonable request.

Keywords: Block Copolymer Particles · Nanoparticles · Particle Functionalization · Seeded Polymerization · Shape Anisotropy

[1] K. Liu, L. Jiang, *Nano Today* **2011**, *6*, 155–175.
[2] a) M. J. York-Duran, M. Godoy-Gallardo, C. Labay, A. J. Urquhart, T. L. Andresen, L. Hosta-Rigau, *Colloids Surf. B* **2017**, *152*, 199–213; b) A. F. Mason, N. A. Yewdall, P. L. W. Welzen, J. Shao, M. van Stevendaal, J. C. M. van Hest, D. S. Williams, L. K. E. A. Abdelmohsen, *ACS Cent. Sci.* **2019**, *5*, 1360–1365.
[3] a) Q. He, K. H. Ku, H. Vijayamohanan, B. J. Kim, T. M. Swager, *J. Am. Chem. Soc.* **2020**, *142*, 10424–10430; b) D.-P. Song, C. Li, W. Li, J. J. Watkins, *ACS Nano* **2016**, *10*, 1216–1223; c) Q. He, H. Vijayamohanan, J. Li, T. M. Swager, *J. Am. Chem. Soc.* **2022**, *144*, 5661–5667.
[4] V. Sharma, A. Sundaramurthy, *ACS Omega* **2019**, *4*, 628–636.
[5] a) M. Okubo, N. Saito, R. Takekoh, H. Kobayashi, *Polymer* **2005**, *46*, 1151–1156; b) T. Higuchi, K. Motoyoshi, H. Sugimori, H. Jinnai, H. Yabu, M. Shimomura, *Macromol. Rapid Commun.* **2010**, *31*, 1773–1778; c) C. Chen, R. A. Wylie, D. Klinger, L. A. Connal, *Chem. Mater.* **2017**, *29*, 1918–1945; d) K. H. Ku, J. M. Shin, H. Yun, G.-R. Yi, S. G. Jang, B. J. Kim, *Adv. Funct. Mater.* **2018**, *28*, 1802961; e) C. K. Wong, X. Qiang, A. H. Müller, A. H. Gröschel, *Prog. Polym. Sci.* **2020**, *102*, 101211.
[6] a) H. Yabu, T. Higuchi, M. Shimomura, *Adv. Mater.* **2005**, *17*, 2062–2065; b) S.-J. Jeon, G.-R. Yi, S.-M. Yang, *Adv. Mater.* **2008**, *20*, 4103–4108; c) D. Klinger, C. X. Wang, L. A. Connal, D. J. Audus, S. G. Jang, S. Kraemer, K. L. Killops, G. H. Fredrickson, E. J. Kramer, C. J. Hawker, *Angew. Chem. Int. Ed.* **2014**, *53*, 7018–7022; *Angew. Chem.* **2014**, *126*, 7138–7142; d) K. H. Ku, Y. Kim, G.-R. Yi, Y. S. Jung, B. J. Kim, *ACS Nano* **2015**, *9*, 11333–11341; e) J. M. Shin, Y. Kim, H. Yun, G.-R. Yi, B. J. Kim, *ACS Nano* **2017**, *11*, 2133–2142; f) A. Steinhaus, T. Pelras, R. Chakroun, A. H. Gröschel, M. Müllner, *Macromol. Rapid Commun.* **2018**, *39*, 1800177; g) J. Lee, K. H. Ku, C. H. Park, Y. J. Lee, H. Yun, B. J. Kim, *ACS Nano* **2019**, *13*, 4230–4237.
[7] a) T. Tanaka, N. Saito, M. Okubo, *Macromolecules* **2009**, *42*, 7423–7429; b) J. Xu, K. Wang, J. Li, H. Zhou, X. Xie, J. Zhu, *Macromolecules* **2015**, *48*, 2628–2636; c) X. Qiang, S. Franzka, G. Quintieri, X. Dai, C. K. Wong, A. H. Gröschel, *Angew. Chem. Int. Ed.* **2021**, *60*, 21668–21672; *Angew. Chem.* **2021**, *133*, 21836–21840; d) K. H. Ku, Y. J. Lee, Y. Kim, B. J. Kim, *Macromolecules* **2019**, *52*, 1150–1157; e) X. Li, J. Li, C. Wang, Y. Liu, H. Deng, *J. Mater. Chem. C* **2019**, *7*, 2535–2540; f) S. Azhdari, F. Herrmann, D. Coban, J. Linders, A. H. Gröschel, *Macromol. Rapid Commun.* **2022**, *43*, 2100932.
[8] a) J. Xu, Y. Yang, K. Wang, J. Li, H. Zhou, X. Xie, J. Zhu, *Langmuir* **2015**, *31*, 10975–10982; b) K. H. Ku, J. M. Shin, M. P. Kim, C.-H. Lee, M.-K. Seo, G.-R. Yi, S. G. Jang, B. J. Kim, *J. Am. Chem. Soc.* **2014**, *136*, 9982–9989; c) M. Xu, K. H. Ku, Y. J. Lee, J. J. Shin, E. J. Kim, S. G. Jang, H. Yun, B. J. Kim, *Chem. Mater.* **2020**, *32*, 7036–7043.
[9] a) R. H. Staff, P. Rupper, I. Lieberwirth, K. Landfester, D. Crespy, *Soft Matter* **2011**, *7*, 10219–10226; b) R. Deng, L. Zheng, X. Mao, B. Li, J. Zhu, *Small* **2021**, *17*, 2006132.
[10] a) J. Lee, K. H. Ku, M. Kim, J. M. Shin, J. Han, C. H. Park, G.-R. Yi, S. G. Jang, B. J. Kim, *Adv. Mater.* **2017**, *29*, 1700608; b) J. Lee, K. H. Ku, J. Kim, Y. J. Lee, S. G. Jang, B. J. Kim, *J. Am. Chem. Soc.* **2019**, *141*, 15348–15355.
[11] a) D. Klinger, M. J. Robb, J. M. Spruell, N. A. Lynd, C. J. Hawker, L. A. Connal, *Polym. Chem.* **2013**, *4*, 5038–5042; b) S. Lee, J. J. Shin, K. H. Ku, Y. J. Lee, S. G. Jang, H. Yun, B. J. Kim, *Macromolecules* **2020**, *53*, 7198–7206; c) G. Quintieri, M. Saccone, M. Spengler, M. Giese, A. H. Gröschel, *Nanomaterials* **2018**, *8*, 1029.
[12] a) B. V. K. J. Schmidt, J. Elbert, D. Scheid, C. J. Hawker, D. Klinger, M. Gallei, *ACS Macro Lett.* **2015**, *4*, 731–735; b) E. J. Kim, J. M. Shin, Y. Kim, K. H. Ku, H. Yun, B. J. Kim, *Polym. Chem.* **2019**, *10*, 2415–2423; c) R. Deng, S. Liu, F. Liang, K. Wang, J. Zhu, Z. Yang, *Macromolecules* **2014**, *47*, 3701–3707; d) Y. Hirai, T. Wakiya, H. Yabu, *Polym. Chem.* **2017**, *8*, 1754–1759; e) L. S. Grundy, V. E. Lee, N. Li, C. Sosa, W. D. Mulhearn, R. Liu, R. A. Register, A. Nikoubashman, R. K.

Prud'homme, A. Z. Panagiotopoulos, R. D. Priestley, *ACS Nano* **2018**, *12*, 4660–4668; f) A. Steinhaus, D. Srivastva, X. Qiang, S. Franzka, A. Nikoubashman, A. H. Gröschel, *Macromolecules* **2021**, *54*, 1224–1233.

[13] Y. J. Lee, H.-E. Kim, H. Oh, H. Yun, J. Lee, S. Shin, H. Lee, B. J. Kim, *ACS Nano* **2022**, *16*, 2988–2996.

[14] a) A. S. Anselmo, L. Lindgren, J. Rysz, A. Bernasik, A. Budkowski, M. R. Andersson, K. Svensson, J. van Stam, E. Moons, *Chem. Mater.* **2011**, *23*, 2295–2302; b) D. Varadharajan, H. Turgut, J. Lahann, H. Yabu, G. Delaittre, *Adv. Funct. Mater.* **2018**, *28*, 1800846; c) H. Turgut, N. Dingenouts, V. Trouillet, P. Krolla-Sidenstein, H. Gliemann, G. Delaittre, *Polym. Chem.* **2019**, *10*, 1344–1356; d) H. Turgut, D. Varadharajan, N. Dingenouts, G. Delaittre, *Macromol. Rapid Commun.* **2018**, *39*, 1800231; e) M. Häckel, L. Kador, D. Kropp, H. W. Schmidt, *Adv. Mater.* **2007**, *19*, 227–231; f) T. Breiner, K. Kreger, R. Hagen, M. Häckel, L. Kador, A. H. Müller, E. J. Kramer, H.-W. Schmidt, *Macromolecules* **2007**, *40*, 2100–2108.

[15] B. V. K. J. Schmidt, C. X. Wang, S. Kraemer, L. A. Connal, D. Klinger, *Polym. Chem.* **2018**, *9*, 1638–1649.

[16] a) J. M. Shin, Y. J. Lee, M. Kim, K. H. Ku, J. Lee, Y. Kim, H. Yun, K. Liao, C. J. Hawker, B. J. Kim, *Chem. Mater.* **2019**, *31*, 1066–1074; b) R. Deng, F. Liang, W. Li, Z. Yang, J. Zhu, *Macromolecules* **2013**, *46*, 7012–7017; c) C. Sinturel, M. Vayer, M. Morris, M. A. Hillmyer, *Macromolecules* **2013**, *46*, 5399–5415; d) A. Baruth, M. Seo, C. H. Lin, K. Walster, A. Shankar, M. A. Hillmyer, C. Leighton, *ACS Appl. Mater. Interfaces* **2014**, *6*, 13770–13781; e) D. Montarnal, N. Delbosc, C. Chamignon, M. A. Virolleaud, Y. Luo, C. J. Hawker, E. Drockenmuller, J. Bernard, *Angew. Chem. Int. Ed.* **2015**, *54*, 11117–11121; *Angew. Chem.* **2015**, *127*, 11269–11273; f) J. G. Son, K. W. Gotrik, C. A. Ross, *ACS Macro Lett.* **2012**, *1*, 1279–1284; g) X. Qiang, X. Dai, A. Steinhaus, A. H. Gröschel, *ACS Macro Lett.* **2019**, *8*, 1654–1659; h) H. Fan, Z. Jin, *Macromolecules* **2014**, *47*, 2674–2681; i) S. Mei, Z. Jin, *Small* **2013**, *9*, 322–329.

[17] K. Parkatzidis, N. P. Truong, M. Rolland, V. Lutz-Bueno, E. H. Pilkington, R. Mezzenga, A. Anastasaki, *Angew. Chem. Int. Ed.* **2022**, *61*, e202113424; *Angew. Chem.* **2022**, *134*, e202113424.

[18] a) J. J. Shin, *Polymer* **2020**, *12*, 2804; b) D. Le, D. Keller, G. Delaittre, *Macromol. Rapid Commun.* **2019**, *40*, 1800551.

[19] a) J.-W. Kim, K.-D. Suh, *Polymer* **2000**, *41*, 6181–6188; b) M. Okubo, J. Izumi, T. Hosotani, T. Yamashita, *Colloid Polym. Sci.* **1997**, *275*, 797–801; c) Y. Asaumi, J. Fujiwara, K. Oyama, M. Rey, N. Vogel, T. Hirai, Y. Nakamura, S. Fujii, *Chem. Lett.* **2020**, *49*, 1282–1285.

[20] a) C. Tang, C. Zhang, J. Liu, X. Qu, J. Li, Z. Yang, *Macromolecules* **2010**, *43*, 5114–5120; b) X. Yu, Y. Sun, F. Liang, B. Jiang, Z. Yang, *Macromolecules* **2019**, *52*, 96–102; c) T. S. Skelhon, Y. Chen, S. A. Bon, *Langmuir* **2014**, *30*, 13525–13532; d) Y. Li, S. Chen, S. Demirci, S. Qin, Z. Xu, E. Olson, F. Liu, D. Palm, X. Yong, S. Jiang, *J. Colloid Interface Sci.* **2019**, *543*, 34–42; e) F. Wurm, A. F. Kilbinger, *Angew. Chem. Int. Ed.* **2009**, *48*, 8412–8421; *Angew. Chem.* **2009**, *121*, 8564–8574; f) B. T. Pham, C. H. Such, B. S. Hawkett, *Polym. Chem.* **2015**, *6*, 426–435.

[21] a) G. Liu, Y. Guan, Y. Ge, L. Xie, *J. Appl. Polym. Sci.* **2011**, *120*, 3278–3283; b) H. Sheu, M. El-Aasser, J. Vanderhoff, *J. Polym. Sci. Part A* **1990**, *28*, 629–651; c) G. Russo, M. Lattuada, *J. Colloid Interface Sci.* **2022**, *611*, 377–389; d) S. A. Shamsudin, T. Mikihito, H. Hirokazu, *Macromol. Symp.* **2017**, *371*, 75–83; e) Q. Yang, K. Loos, *Polymer* **2017**, *9*, 525; f) W. I. Park, S. Tong, Y. Liu, I. W. Jung, A. Roelofs, S. Hong, *Nanoscale* **2014**, *6*, 15216–15221.

[22] Y. Seo, D. Woo, L. Li, W. Li, J. K. Kim, *Macromolecules* **2021**, *54*, 7822–7829.

[23] a) M. Albuszis, P. J. Roth, W. Pauer, H.-U. Moritz, *Polym. Chem.* **2016**, *7*, 5414–5425; b) S.-X. Li, L.-R. Feng, X.-J. Guo, Q. Zhang, *J. Mater. Chem. C* **2014**, *2*, 3517–3520; c) M. Albuszis, P. J. Roth, F. Exnowitz, D. L. Wong, W. Pauer, H.-U. Moritz, *Polym. Chem.* **2016**, *7*, 1168–1180; d) R. H. Staff, J. Willersinn, A. Musyanovych, K. Landfester, D. Crespy, *Polym. Chem.* **2014**, *5*, 4097–4104.

[24] L. Navarro, A. F. Thünemann, D. Klinger, *ACS Macro Lett.* **2022**, *11*, 329–335.

[25] D. Liu, Y. Lin, K. Gong, H. Bo, D. Li, Z. Zhang, W. Chen, *RSC Adv.* **2021**, *11*, 38316–38324.

Manuscript received: June 1, 2022
Accepted manuscript online: July 4, 2022
Version of record online: July 21, 2022

Angewandte Chemie
Eine Zeitschrift der Gesellschaft Deutscher Chemiker

Supporting Information

Regioselective Seeded Polymerization in Block Copolymer Nanoparticles: Post-Assembly Control of Colloidal Features

*L. Navarro, A. F. Thünemann, T. Yokosawa, E. Spiecker, D. Klinger**

Content

Materials

All chemical reagents purchased from commercial sources were used without further purification unless otherwise is specified. Poly(styrene-*block*-2-vinyl pyridine) (PS-*b*-P2VP) with a molecular weight of 102k-97 kDa was purchased from Polymer Source Inc. For other reagents, the commercial suppliers are listed as follows: Cetyl trimethyl ammonium bromide (CTAB, Sigma Aldrich, ≥99%), toluene (Fisher, ACS grade), chloroform (Fisher, HPLC grade), iodine (ACROS Organics, pure), 2,2′-azobis-isobutyronitrile (AIBN, Fluka), polystyrene homopolymer (*h*PS, GPC standard, 90 kDa, Sigma Aldrich), 1,4-dibromobutane (DBB, Sigma Aldrich), 4-vinylbenzyl chloride (Sigma Aldrich, 90%), ethynylferrocene (FCN-alkyne, 97%, Sigma Aldrich), tetramethyl rhodamine alkyne (TAMRA alkyne, ≥95%, Sigma Aldrich), tris(benzyltriazolylmethyl)amine (TBTA, TCI Chemicals), $CuSO_4 \cdot 5H_2O$ (Sigma Aldrich). Styrene (St, Sigma Aldrich) was distilled prior to use. Methyl methacrylate (MMA, Sigma Aldrich) was filtered over basic aluminum oxide. 6-hydroxy-N,N,N-triethylhexadecan-1-ammonium bromide (CTEAB-OH) was synthesized according to the literature. [1] Chloroform, ethanol, methanol, tert-buthanol (t-BuOH) and di-methylsulfoxide (DMSO) were purchased from Fisher Scientific.

Instrumentation

Transmission electron microscopy (TEM)

To remove the excess of surfactants, the particles were purified by 3 cycles of centrifugation (6000 rpm, 5 min) and resuspension in Milli-Q water. TEM samples were prepared by applying a 10 µL droplet of the purified particle solution on a carbon-coated copper grid (400 meshes, Quantifoil Micro ToolsGmbH, Großlöbichau, Germany) for 45 s. Excess liquid was then removed by blotting with filter paper. The samples were allowed to dry in air overnight and were stained using an iodine chamber for 15 minutes. Measurements were performed in the TEM mode of a Hitachi Scanning Electron Microscope (SU8030, Hitachi High-Technologies Corporation, Tokyo, Japan) with a working voltage of 30.0 kV.

Small-angle X-ray scattering (SAXS)

SAXS measurements were performed using a modified Xeuss 2.0 instrument (Xenocs, Sassenage France). X-rays were generated from a microfocus X-ray tube with a copper target, followed by a multilayer optic to parallelize and monochromatize the X-ray beam to a wavelength of 0.154 nm. The instrument has a vacuum motorized detector (Eiger 1M, Dectris, Baden-Daettwil, Switzerland). The samples with a volume of 4 ml were probed within a flow-through cell under constant flow to avoid sedimentation. The sample cell was equipped with SiN windows. The resulting data were processed using the DAWN software package according to standardized procedures.[2]

The simplest model we found for interpretation of the scattering profiles is that the scattering is given by an q^4-scaling (Porod's law), peak functions and a constant background *b*. This composite model is given by equation (1):

$$I(q) = a\, q^{-4} + \sum_{i=1}^{2} I_{p,i}(q) + b \qquad (1)$$

Exploration of the data reveals that neither Gaussian nor Lorentzian curve profiles provide satisfactory curve fits for both data sets. Therefore, we utilized a pseudo-Voit function for $I_{p,i}(q)$, which is a linear combination of a Gaussian and Lorentzian profile as equation (2):

$$I_{p,i}(q) = \frac{(1-\alpha_i)A_i}{\sigma_{G,i}\sqrt{2\pi}} \exp\left[-\frac{(q-q_i)^2}{2\sigma_{G,i}^2}\right] + \frac{\alpha_i A_i}{\pi}\left[\frac{\sigma_i}{(q-q_i)^2+\sigma_i^2}\right] \quad (2)$$

Here α_i is the relative fraction of the Gaussian, A_i is the peak amplitude and q_i is the position of the peak maximum. The $\sigma_{G,i} = \sigma_i/\sqrt{2\ln 2}$ is the width parameter of the Gaussian where σ_i is the width parameter of the Lorentzian. The width definition of the Gaussian $\sigma_{G,i}$was chosen so that the full width at half maximum of the peak is $2\sigma_i$. The respective fitting parameters are shown in Table S1 for the crosslinked particles and the same particles after seeded polymerization with 200 wt% and 500 wt% styrene.

Table S1. Fitting parameters for $I_{p,i}(q)$according to equation (2) for SAXS scattering curves of pristine particles and crosslinked articles after seeded polymerization with 200 wt% and 500 wt% styrene.

Crosslinked particles		**Seeded particles**			
		200 wt% styrene		**500 wt% styrene**	
variable	**value**	**variable**	**value**	**variable**	**value**
V1_amplitude	15.0	**V1_amplitude**	25.0	**V1_amplitude**	45.0
V1_center	0.080	**V1_center**	0.049	**V1_center**	0.039
V1_sigma	0.01	**V1_sigma**	0.008	**V1_sigma**	0.008
V1_fraction	1.0	**V1_fraction**	0.5	**V1_fraction**	0.35
V1_fwhm	0.020	**V1_fwhm**	0.016	**V1_fwhm**	0.016
V1_height	477.5	**V1_height**	1231.3	**V1_height**	2344.1
V3_amplitude	0.35	**V3_amplitude**	1.45	**V3_amplitude**	2.45
V3_center	0.24	**V3_center**	0.147	**V3_center**	0.117
V3_sigma	0.03	**V3_sigma**	0.04	**V3_sigma**	0.024
V3_fraction	1.0	**V3_fraction**	0.50	**V3_fraction**	0.35
V3_fwhm	0.06	**V3_fwhm**	0.08	**V3_fwhm**	0.048
V3_height	3.71	**V3_height**	14.3	**V3_height**	42.54
				V5_amplitude	0.45
				V5_center	0.195
				V5_sigma	0.04
				V5_fraction	0.35
				V5_fwhm	0.08
				V5_height	4.69
a	0.004	**a**	0.004	**a**	0.004
bkg	0.05	**bkg**	0.03	**bkg**	0.02
qmin	0.02	**qmin**	0.02	**qmin**	0.019
dmax	160	**dmax**	160	**dmax**	170
lc	630	**lc**	790	**lc**	790
d	79	**d**	130	**d**	160

Energy-dispersive X-ray spectroscopy (EDX)
The samples were prepared by dispersing the suspensions on a carbon-coated gold grid, the excess was removed by blotting with a filter paper and finally air-dried for 12 h. Energy-dispersive X-ray spectroscopy combined with scanning TEM (STEM-EDX) measurements were carried out using a double-corrected FEI Titan Themis3 300 microscope (Thermo Fisher Scientific Inc.) equipped with a Super-X detector and operated at 300 kV.

Spectroscopic techniques
NMR. ^{1}H spectra were recorded at 300 K on a JEOL ECP 500 spectrometer operating at 500 MHz and on a JEOL ECZ600 spectrometer operating at 600 MHz.

ATR-FTIR. IR spectra by attenuated total reflection (ATR) were recorded on a PerkinElmer Spectrum Two spectrometer measuring between 4000 and 650 cm^{-1} (PerkinElmer, Waltham, United States of America). All data were processed using Spectrum (10.4.4) from PerkinElmer.

UV/Vis. UV/Vis spectroscopy was performed on a Tecan Spark plate reader (Tecan Trading AG, Männedorf, Switzerland). All data were processed using the software SparkControl.

Gel permeation chromatography (GPC)
The number-average molecular weights (M_n) and molecular weight distributions (M_w/M_n) of polymer samples were determined using a customized GPC system (PSS Polymer Standard Service GmbH, Mainz, Germany), operating with DMF at 50 °C and comprising two PSS SDV linear M 5 µm particle size columns (5 cm and 30 cm) connected in series to a PSS SECcurity RI differential refractometer detector. HPLC-grade DMF with 10 mmol lithium bromide was used as eluent at a flow rate of 1.0 mL min^{-1}. Calibration was conducted using poly(methyl methacrylate) standards (M_n = 600–1 600 000 g mol^{-1}). Polymer sample solutions (1.5 mg ml^{-1}) were prepared in the GPC eluent and filtered (PTFE, 450 µm) prior to injection. Chromatograms were processed using the PSS WinGPC UniChrom software.

Synthetic Procedures

Preparation of striped ellipsoidal particles
PS-*b*-P2VP striped ellipsoidal particles were prepared by the emulsion-solvent evaporation method, as previously reported.[1] Two aqueous stock solutions of CTEAB-OH (1 mg g^{-1}) and CTAB (1 mg g^{-1}) were mixed in a ratio of CTEAB-OH/CTAB = 70 / 30 (wt/wt) to give 5 g surfactant solution. Milli-Q water (5 g) was added to obtain a total of 10 g of continuous phase with an overall surfactant concentration of 0.05 wt%. PS-*b*-P2VP solution was prepared in chloroform with a concentration of 1 wt% and 1.5 g was added to the surfactant solution. Emulsification was performed by vortexing and sonication. Chloroform was evaporated by stirring the emuslions open to air at 32 °C for 48 h. The resulting particle suspension was washed three times by cycles of centrifugation and resuspension in Milli-Q water. To determine particle morphology the samples were analyzed by TEM.

Crosslinking of P2VP domains

After particle synthesis, PS-*b*-P2VP particle dispersions were diluted with deionized water to a final volume of 15 mL. Crosslinking of P2VP domains was performed with 1,4-dibromobutane (DBB). Two DBB concentrations were evaluated to vary the crosslinking density: 50 mol% and 100 mol% of DBB with respect to the 2VP units. For this, 300 µL of a solution of DBB in methanol (12.6 mg ml^{-1} for 50 mol%, and 25.3 mg mL^{-1} for 100 mol%) were added to 5 mL of the diluted particle solution. The dispersion was stirred at 60°C for 48 h. Afterwards, methanol was evaporated by stirring the dispersion in an open vial for 48 h at room temperature. Crosslinking was confirmed by acidifying the particle dispersions to pH 3 and using TEM to demonstate structural stability.

Seeded polymerization

PS-*b*-P2VP striped ellipsoidal particles were used for seeded polymerization using St as monomer and AIBN as radical initiator. For this, a suspension of pre-formed particles (1.5 mg g^{-1}) was de-gassed by argon bubbling. Subsequently, a specific amount of St (containing 0.5 wt% of AIBN) was added via micropipette. After brief sonication (1 min), the particles were left to swell overnight in a sealed vial. Polymerization was started by placing the vial in a preheated oil bath at 70 °C and conducted for 24 h under stirring. Finally, the vial was opened to the air to stop the polymerization and the open dispersion was stirred (12 h, room temperature) to evaporate un-reacted monomer. The resulting particle suspension was washed three times by cycles of centrifugation and resuspension in Milli-Q water. To examine particle morphology, the samples were analyzed by TEM. Control experiments were performed under the same conditions but without the incorporation of a radical initiator.

Particle functionalization via Cu(I)-catalyzed azide/alkyne cycloaddition (CuAAC)

Synthesis of 4-vinylbenzyl azide (VBA)

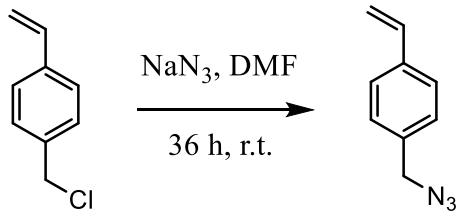

To a solution of 4-vínylbenzyl chloride (10.8 mL, 7.7 mmol) in DMF (150 mL) sodium azide (15 g, 23.1 mmol) was added. The suspension was stirred for 36 h at room temperature before diluting with 300 mL water. The product was extracted with diethyl ether (3 X 300 mL). The organic phase was washed with brine (3 X 200 mL) and dried over $MgSO_4$ before evaporating the solvent in vacuum. The product (12.1 g, 7.6 mmol, 99%) was obtained as an orange oil.

'H-NMR (400 MHz, DMSO-d6) δ/ppm = 7.48-7.45 (m, 2 H, 111), 7.31-7.28 (m, 2 H, ArH), 6.73 (dd, 1 H, J= 17.4 Hz, J= 10.8 Hz, Ar-$CH=CH_2$), 5.80 (dd, 1 H, J= 17.4 Hz, J= 0.9 Hz, Ar-$CH=CH_2$), 5.32 (dd, 1 H, J= 10.8 Hz, J=0.9 Hz, Ar-$CH=CH_2$), 4.35 (s, 2H, Ar-CH_2C1).

Preparation of reactive particles by seeded copolymerization of St and VBA

Crosslinked particles (100 mol% DBB) were subjected to seeded copolymerization with a mixture of St and VBA (ratio c_{St}/c_{VBA} = 90:10 wt/wt; total monomer content $c_{St} + c_{VBA}$ = 500 wt%; 0.5 wt% AIBN). After polymerization (70°C, 24 h), the particle suspension was purified by 4 cycles of centrifugation (6000 rpm, 5 min) and re-suspension in Milli-Q water. The solid content of the final dispersion was determined by gravimetrical analysis after freeze-drying.

CuAAC reaction with TAMRA-alkyne.

Freeze-dried reactive particles were resuspended in 1 mL of Milli-Q water (1 mg·mL^{-1}). Ascorbic acid (0.063 mg) was added, and the suspension was bubbled with argon under sonication. A DMSO stock solution of TAMRA-alkyne was prepared (2.8 mg mL^{-1}) and different volumes were added to reach final concentrations of 1.4, 2.1, 2.8 and 3.5 µg mL^{-1} within the particle suspension. 1 eq of $CuSO_4.5H_2O$ and 2 eq of TBTA were added (equivalents w.r.t. azide groups - assuming quantitative VBA introduction during the seeded polymerization). The mixture was stirred at room temperature for 24 h in a sealed vial. For each concentration of TAMRA-alkyne a control reaction was performed under the same conditions but without the incorporation of $CuSO_4·5H_2O$. Functionalized particles were purified by cycles of centrifugation (6000 rpm, 5 min) and re-suspension in Milli-Q water until TAMRA was no longer detected by UV spectroscopy in the supernatant.

CuAAC reaction with FCN-alkyne

Freeze-dried reactive particles were resuspended in 0.500 mL of Milli-Q water (2 mg·mL^{-1}). Ascorbic acid (0.063 mg) was added, and the suspension was bubbled with argon under sonication. 1 eq of FCN-alkyne (w.r.t. azide groups) was dissolved in 0.500 mL of t-BuOH and degassed by bubbling with argon under sonication. The t-BuOH solution was added to the aqueous particle dispersion containing the ascorbic acid. 1 eq of $CuSO_4·5H_2O$ and 2 eq of TBTA were used to initiate the reaction in a sealed vial. After stirring the mixture for 24 h at room temperature, the particles were purified by cycles of centrifugation (6000 rpm, 5 min) and re-suspension in 1:1 Milli-Q water/t-BuOH. The particles were finally resuspended in Milli-Q water.

Particle preparation through blending with *h*PS

Incorporation of *h*PS (90 kDa) during particle preparation was evaluated through the addition of different homopolymer contents to the PS-*b*-P2VP solution. For this, stock solutions of *h*PS and PS-*b*-P2VP were prepared in chloroform (each 1 wt%). Mixing the stock solutions in different proportions allowed to adjust the *h*PS content (see Table S2). 100 µL of the blend solution were emulsified in 1 mL of the aqueous continuous phase (30% of CTAB and 70% of CTEAB-OH, total surfactant concentration: 0.05 wt%). After emulsification, the solvent was evaporated by stirring at room temperature for 24 h. The particles were then purified by cycles of centrifugation and resuspension in Milli-Q water. Particle morphology was evaluated by TEM.

Table S2. *h*PS / PS-*b*-P2VP blend compositions for preparation of particles.

PS-*b*-P2VP / *h*PS	**PS-*b*-P2VP [µL]***	***h*PS [µL]***
55 / **45**	55	45
60 / **40**	60	40
65 / **35**	65	35

*volume of a 1 wt% stock solution in chloroform

Supplemental Data and Figures

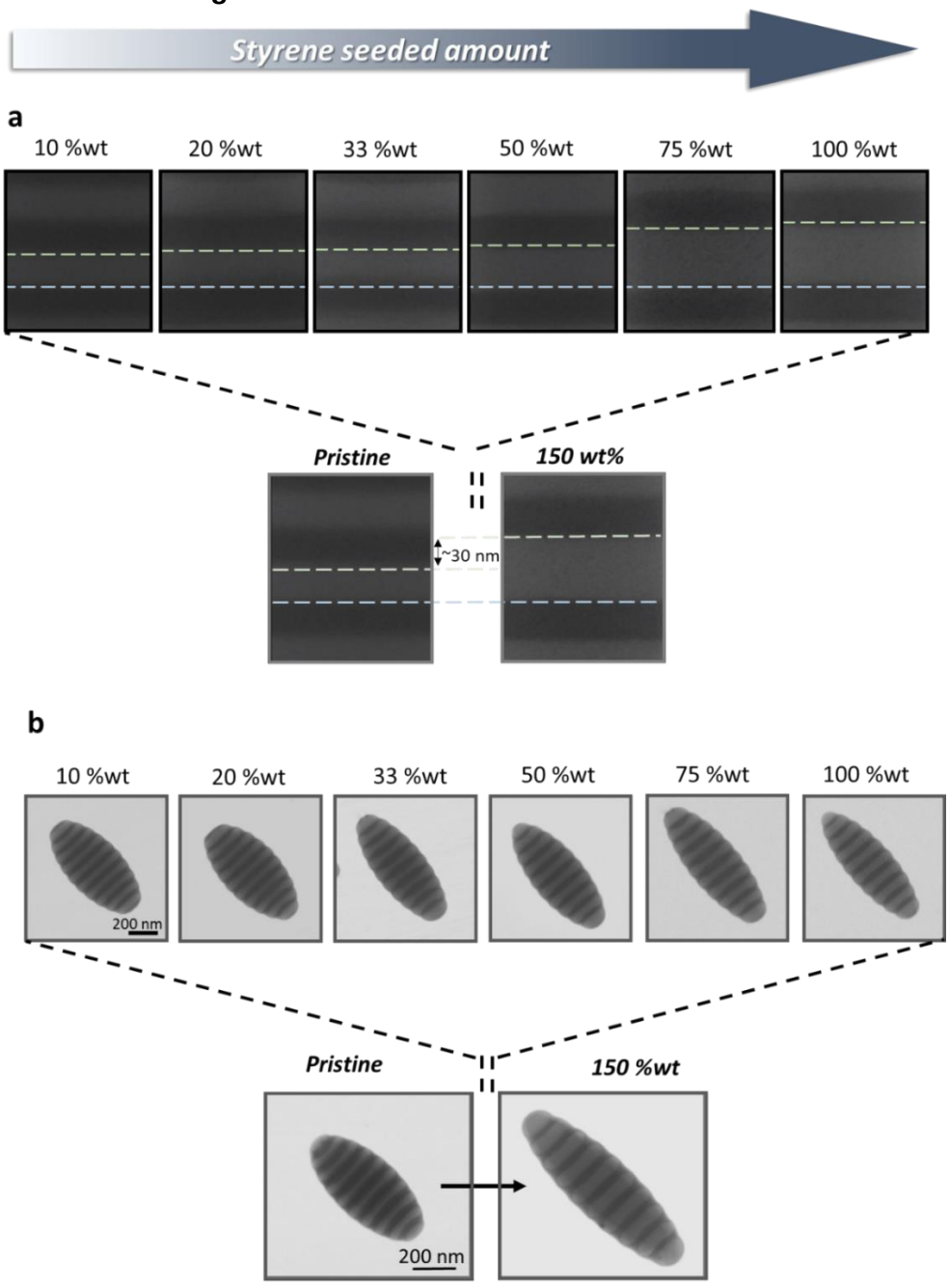

Figure S1. Evolution of morphology and shape of PS-*b*-P2VP particles seeded with different amounts of St. a) TEM pictures of the particle middle section show a selective increment in the thickness of the PS domain over the P2VP domain. This trend increases with the amount of St used in the seeded polymerization. b) TEM pictures of individual particles show particle elongation as result of the PS domain expansion. This trend also increases with c_{St}.

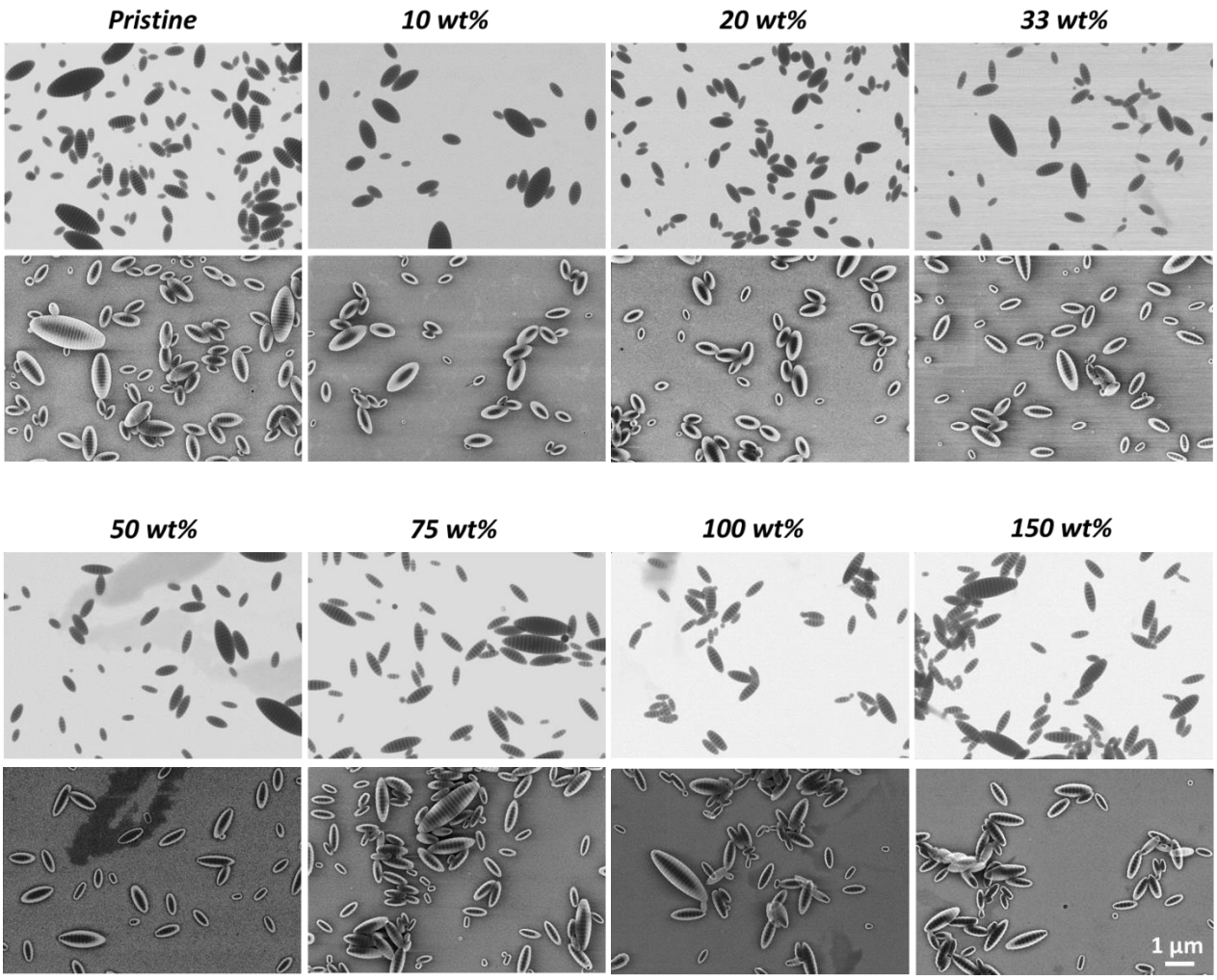

Figure S2. Low magnification TEM and SEM pictures of PS-b-P2VP particles after seeded polymerization with varying styrene contents. All pictures have the same magnification, represented by the scale bar in the bottom right of the image.

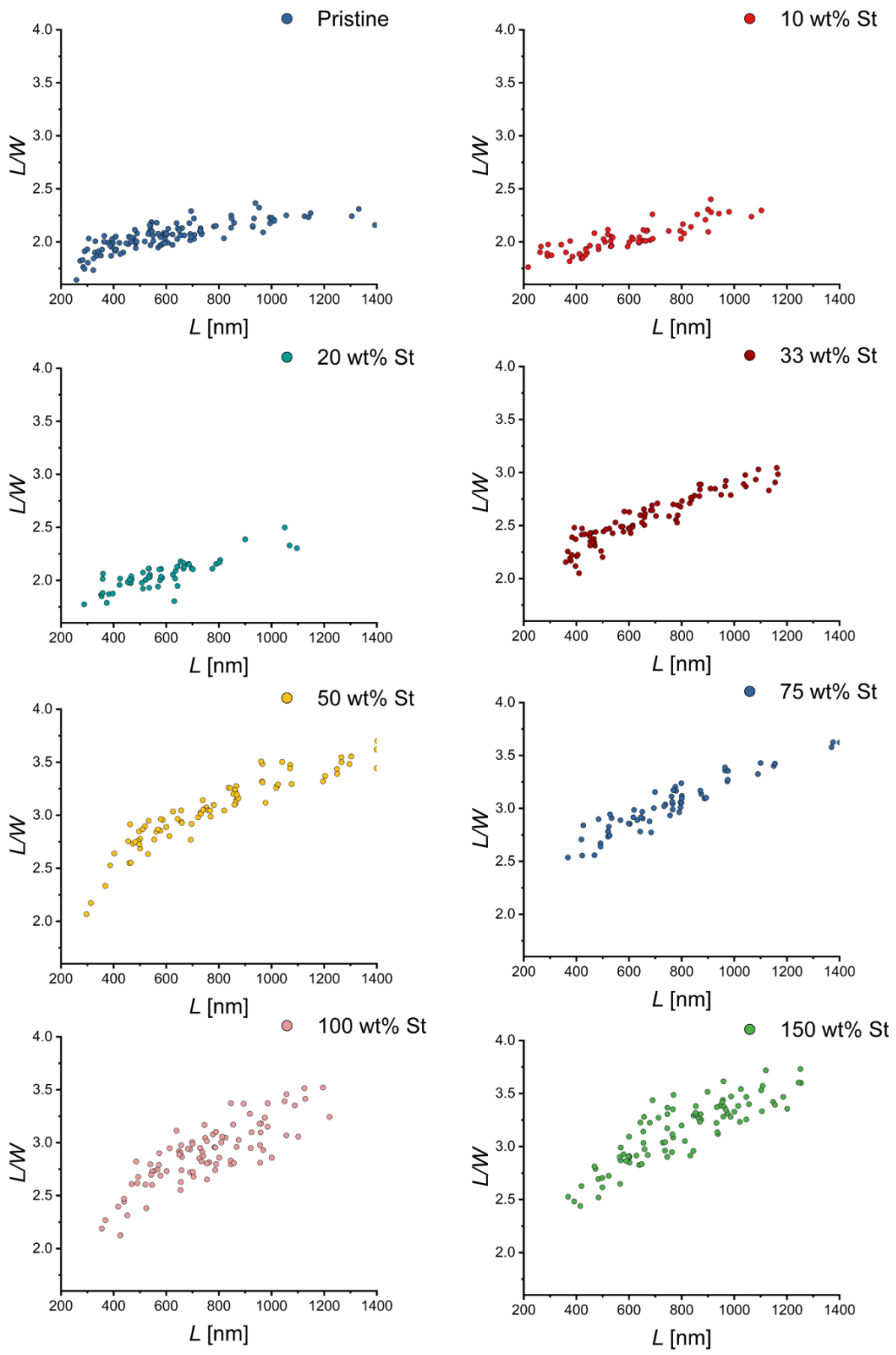

Figure S3. Aspect ratio (AR = L/W) of PS-b-P2VP particles after seeded polymerization with different amounts of styrene. Each graph depicts the dependence of *AR* on particle size (described by *L*).

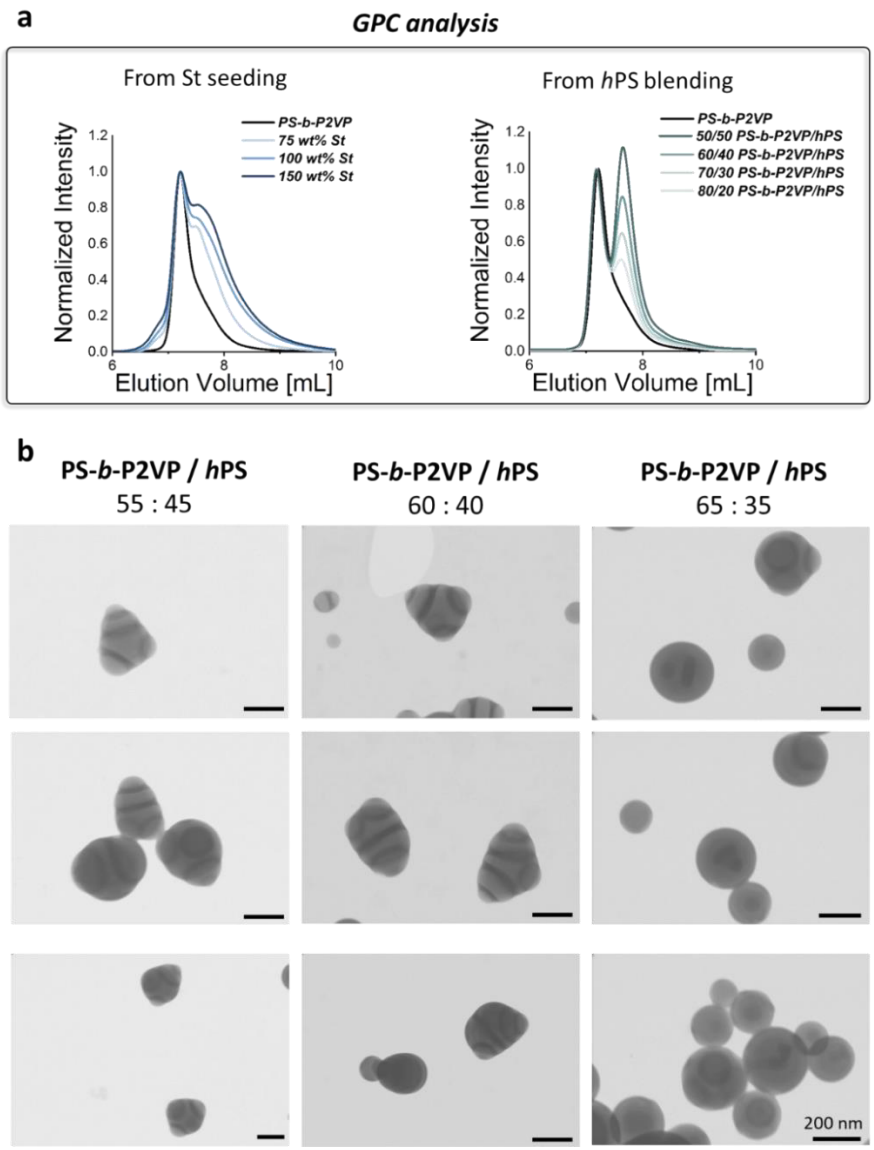

Figure S4. Incorporation of *h*PS during particle self-assembly. (a) GPC analysis of the polymer mixtures. Left panel: Particles after seeded polymerization with styrene were purified by centrifugation, freeze-dried and dissolved in DMF to enable GPC evaluation. A low molecular weight shoulder at the PS-*b*-P2VP peak indicates the formation of PS (90 kDa) through seeded polymerization. Right panel: To mimic the PS-*b*-P2VP/*h*PS blend composition after seeded polymerization, control polymer blends were prepared with a preformed *h*PS standard (90 kDa, Sigma Aldrich) and PS-*b*-P2VP. The elution profiles show that a 60:40 blend (PS-*b*-P2VP/*h*PS) can mimic the particle composition after seeded polymerization with 150 wt% of St. (b) Control particles were prepared from evaporation-induced phase separation of PS-*b*-P2VP/*h*PS blends. Investigated compositions were 55:45, 60:40, and 65:35 of PS-*b*-P2VP/*h*PS. TEM images show that particles don't exhibit an ellipsoidal shape and lamellae morphology. Increasing the volume of PS by blending causes a different morphology due to a changed in the volume ratio between PS and P2VP segments.

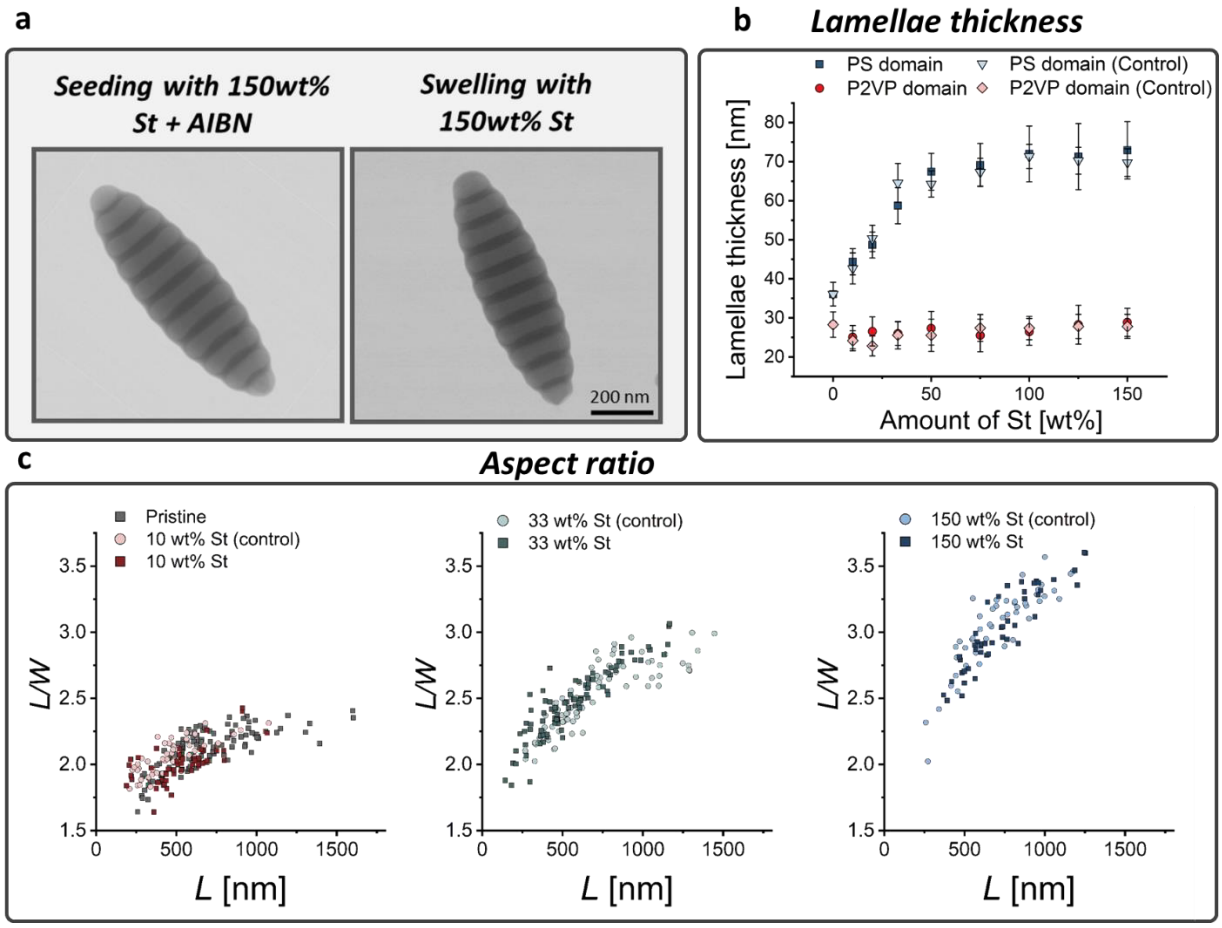

Figure S5. Control experiments to the seeded polymerization were performed under the same conditions but without the initiator. For this, particles were swollen overnight with different amounts of St (without AIBN) followed by incubation at 70 °C for 24 h and evaporation of St for stirring at room temperature for 12 h. a) TEM pictures of a seeded particle (left) and swollen particle (right) with 150 wt% of St show similar shape and inner morphology. b) Lamellae thickness increases similarly with c_{St} for seeded particles and control particles. c) No differences in particle aspect ratio (AR = L/W) are observed for PS-*b*-P2VP particles after seeded polymerization or after reversible swelling with styrene (control samples). However, AR still varies with different amounts of styrene. Each graph depicts the dependence of AR on particle particle size (described by *L*).

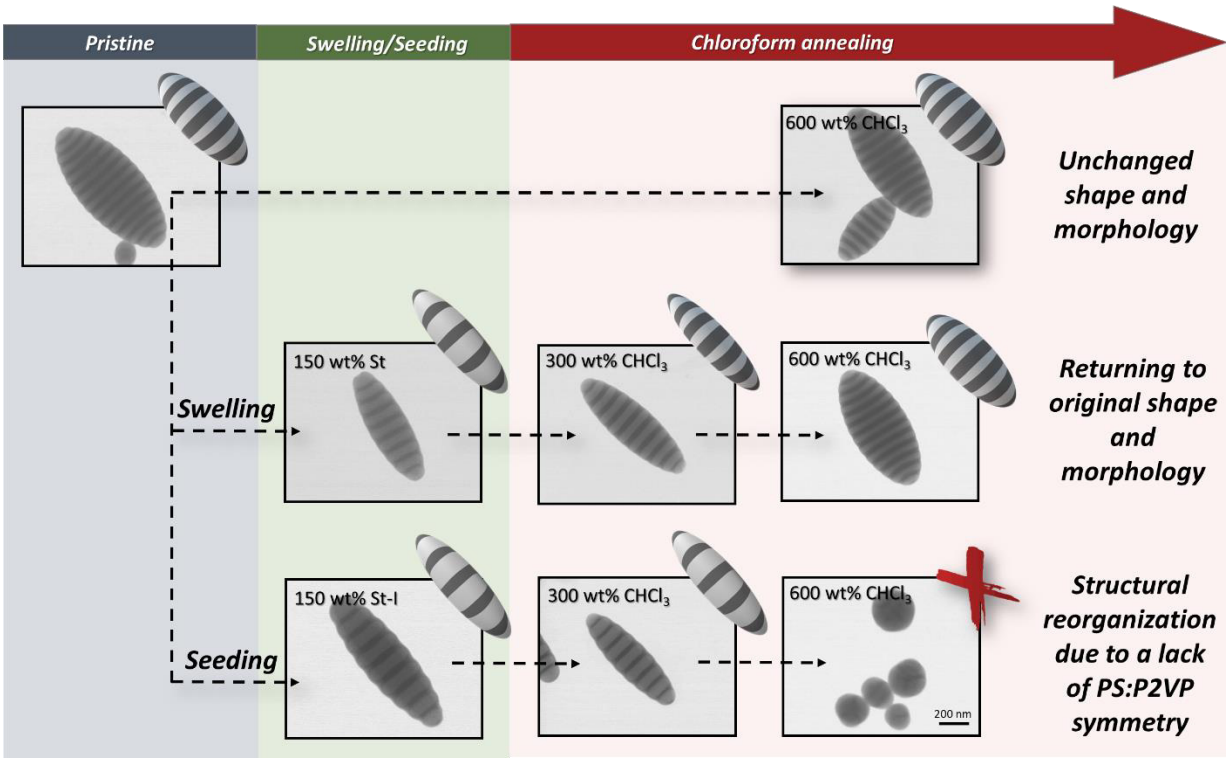

Figure S6. Influence of solvent annealing on shape and morphology of different particles: pristine particles, seeded particles and swollen control particles. All particles were annealed in aqueous dispersion by addition of chloroform as a good solvent for both segments (PS and P2VP). For this, particles were first swollen with chloroform overnight. Afterwards, the solvent was evaporated by stirring the aqueous dispersion at 32 °C for 48 h. For pristine particles, it was observed that particles remain unchanged after chloroform annealing. In contrast, control particles (swollen with styrene) show a progressive return towards the original shape upon chloroform annealing. It is assumed that swelling with chloroform mobilizes both domains and enables BCP restructuring similar to the initial phase separation during particle preparation. Thus, these experiments suggest that no polymerization occurs during the control experiment. For particles after seeded polymerization, a pronounced structural reorganization is observed. Due to polymerization of styrene inside the PS domains, the PS/P2VP volume ratio is shifted to an excess of PS volume. As a result, solvent annealing gives structures that deviate from the lamellar morphology, which requires symmetric PS/P2VP volume ratios. Similar particle morphologies were obtained for the preparation of particles from PS-*b*-P2VP / *h*PS of similar composition (see Figure S5b).

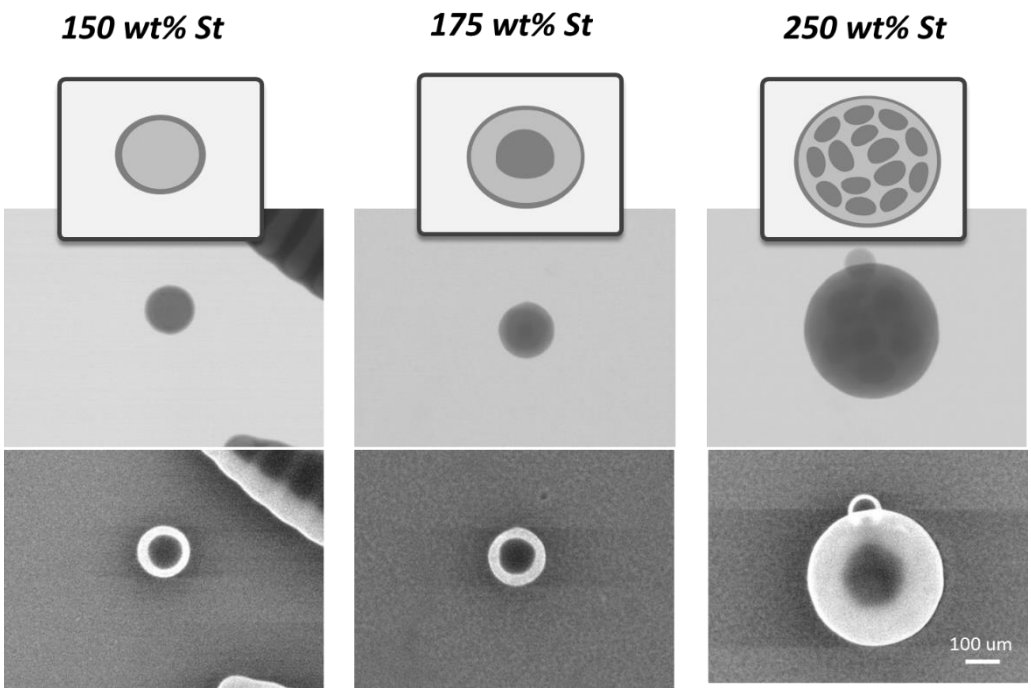

Figure S7. TEM and SEM pictures of disintegrated particles corresponding to 150, 175 and 250 wt% addition of St.

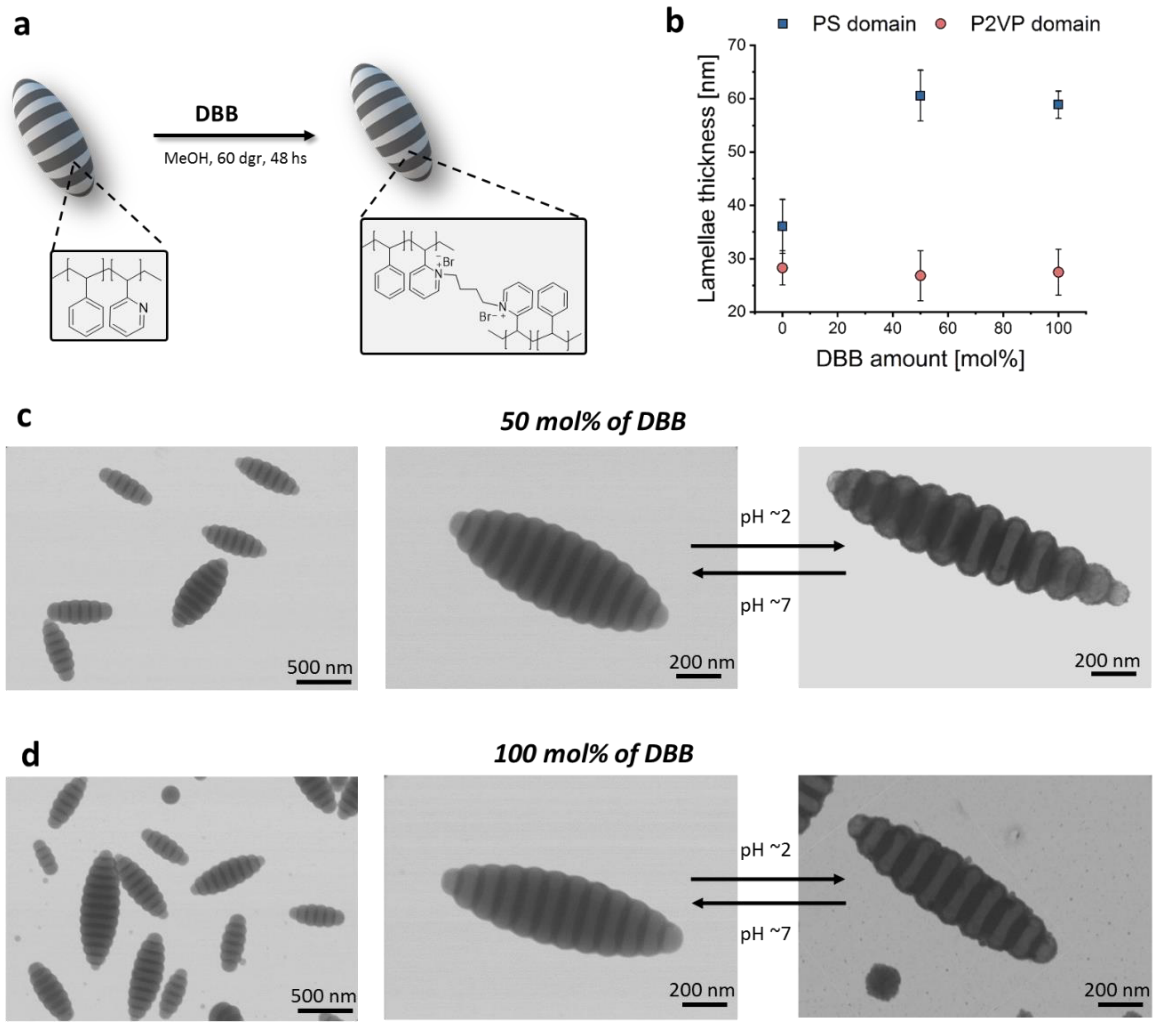

Figure S8. Crosslinking the P2VP domains with 50 and 100 mol% of DBB (with respect to 2VP units). (a) Schematic representation of the covalent crosslinking reaction. (b) Dependence of lamellar thickness on DBB amount: an expansion of the PS domains is observed after the addition of DBB due to a change in the surface affinity of the BCP.[3] TEM images show the influence of pH on the morphology of particles crosslinked with (c) 50 mol% DBB or (d) 100 mol% DBB.

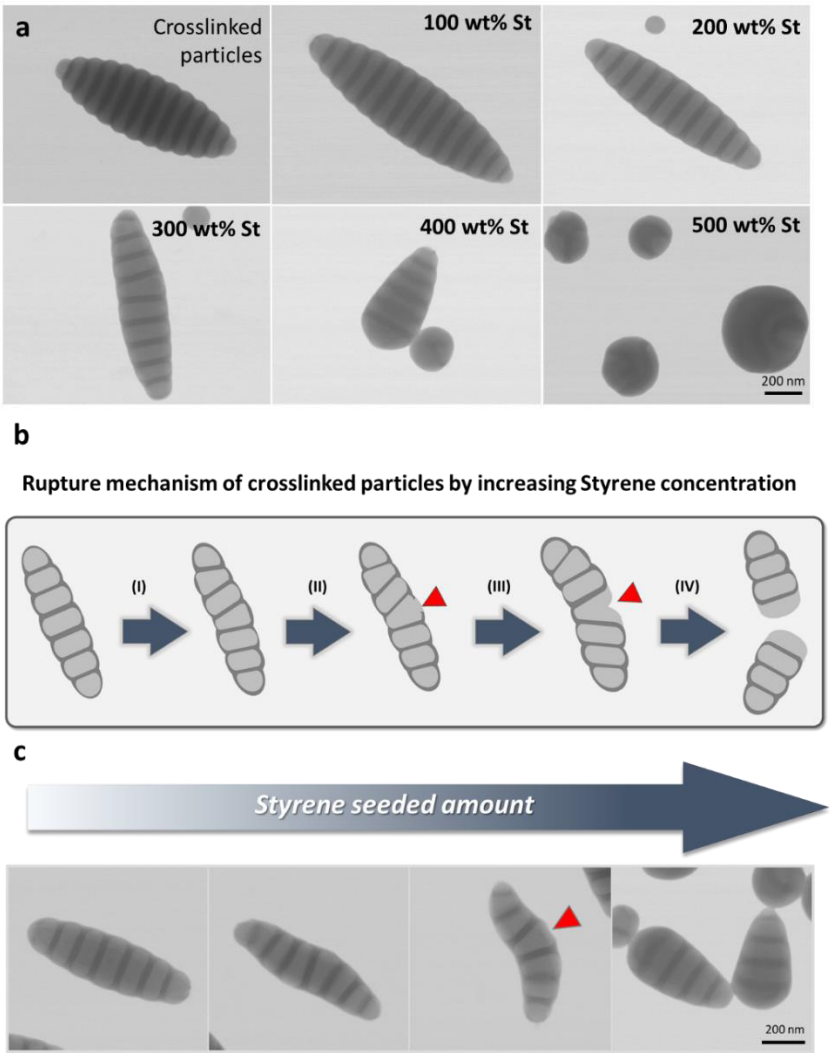

Figure S9. Seeded polymerization of styrene in PS-*b*-P2VP particles (crosslinked with 50 mol% of DBB). (a) TEM images of particles after using different amounts of styrene for the seeded polymerization. (b) Schematic representation of particle disassembly upon increasing c_{St} during the seeded polymerization. It is assumed that P2VP crosslinking causes partial migration of the P2VP segments to the particle surface. This creates a crosslinked P2VP mesh that surrounds discrete PS domains. Before the seeded polymerization, styrene molecules are able to penetrate the P2VP mesh and accumulate in the PS domains. Upon polymerization, the PS domain thickness increases and the P2VP mesh on the outside stretches. (I) With increasing amount of styrene, we observe an asymmetric increment in the PS domain thickness which translates to bending of the particles. (II and III) When increasing c_{St} over 400 wt% we started to observe particle disintegration into conic structures. Here, we suggest that the crosslinking density of the P2VP mesh is not enough to withstand the stress that is caused by the PS expansion. Thus, rupture of the P2VP mesh on the surface is suggested. (IV) Further increasing the amount of styrene leads to complete P2VP rupture and the disintegration into conic structures. (c) TEM images of particles for different c_{St} support the suggested mechanism.

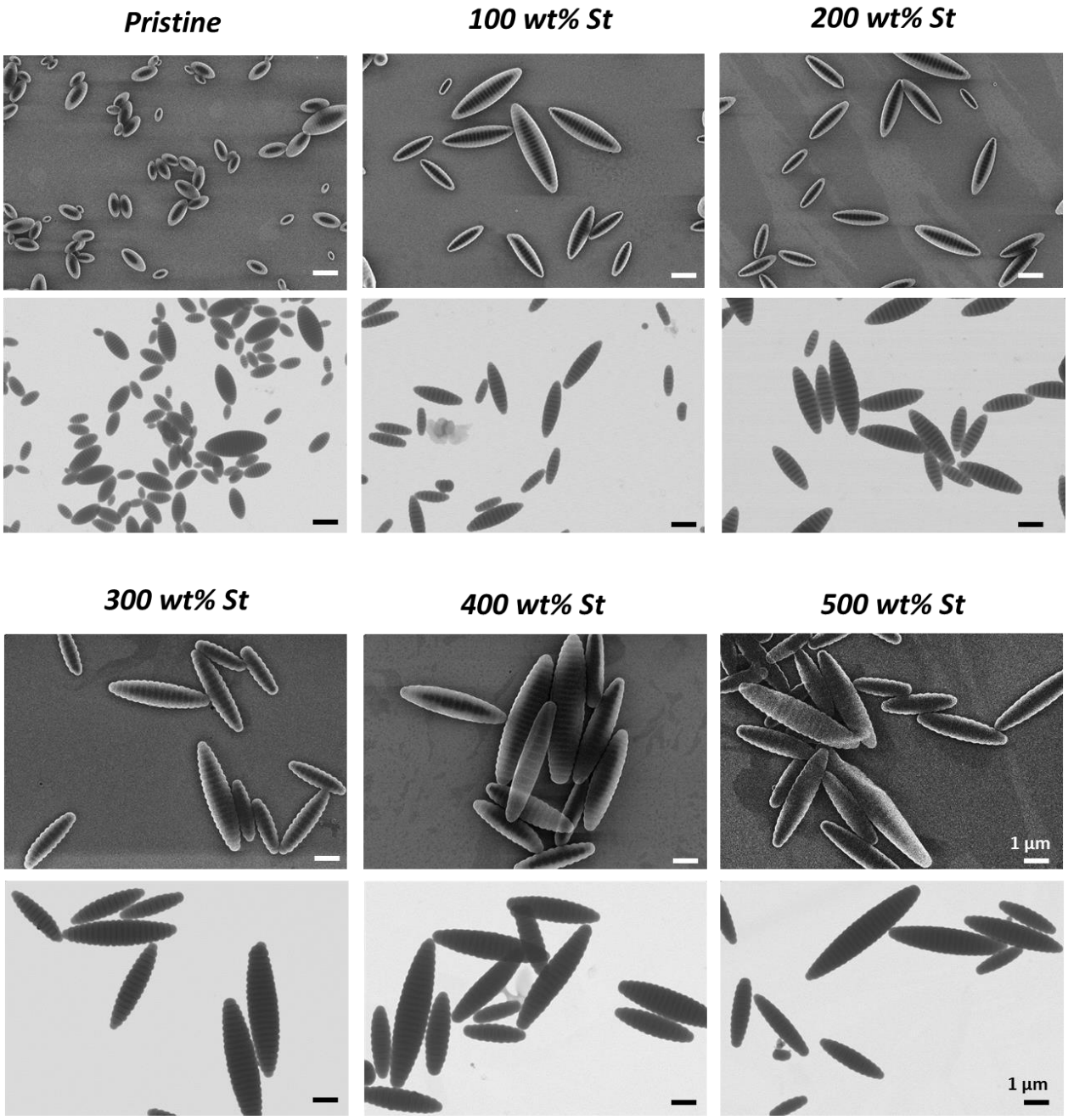

Figure S10. Low magnification TEM and SEM pictures of PS-b-P2VP particles (crosslinked with 100 mol% DBB) after seeded polymerization with varying styrene contents. All pictures have the same magnification, represented by the scale bar in the bottom right of the image.

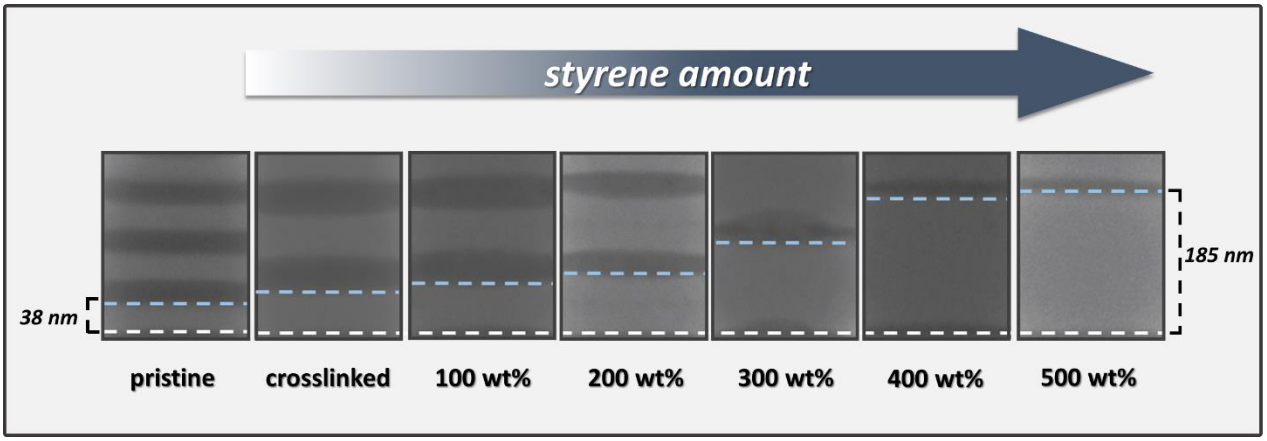

Figure S11. Lamella progression by covalent stabilization of the PS-*b*-P2VP ellipsoids (P2VP crosslinking with 100 mol% DBB). Direct comparison of lamella evolution upon increasing c_{St} shows a significantly increment in the thickness of PS domain with styrene content.

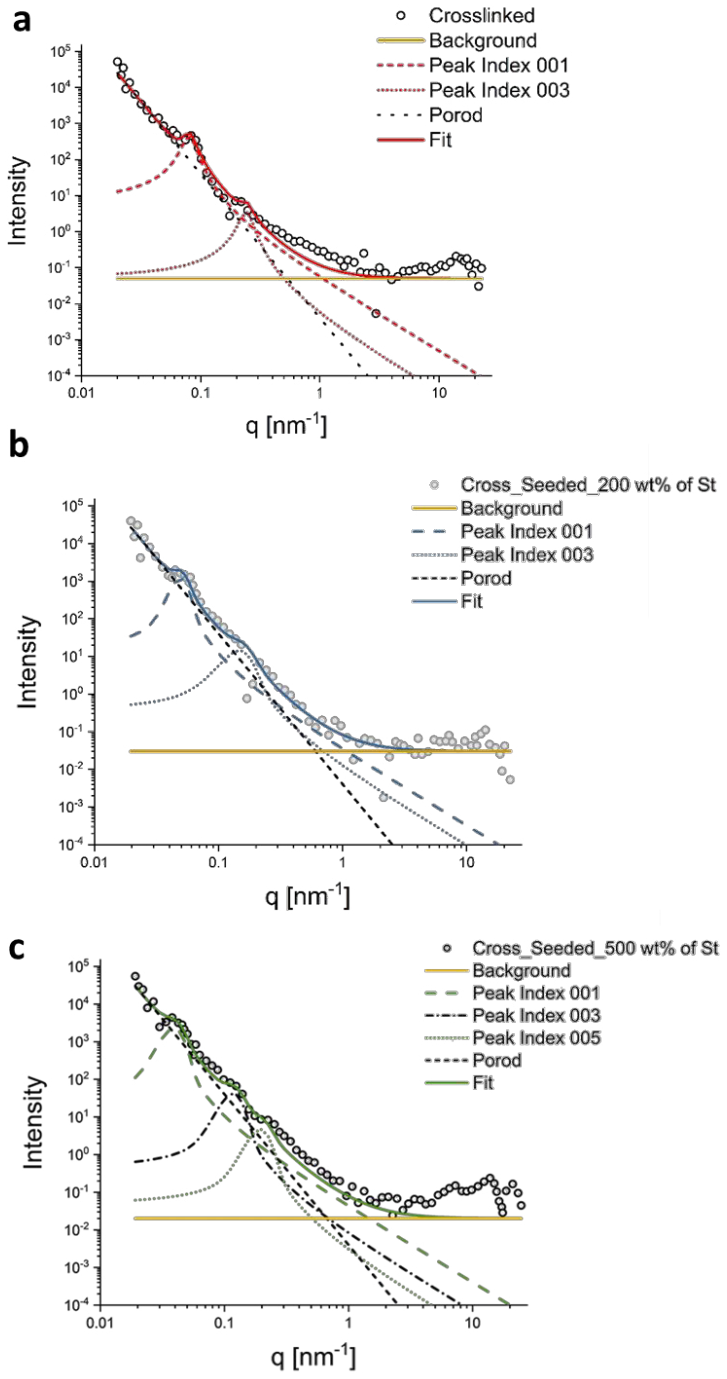

Figure S12. Small angle x-ray analysis of crosslinked particles before and after seeded polymerization with styrene. Scattering pattern of (a) crosslinked particles (100 mol% DBB), (b) crosslinked particles after seeded polymerization with 200 wt% of styrene and (c) crosslinked particles after seeded polymerization with 500 wt% of styrene. All Figures include the actual data and the respective fits with the individual contributions as described earlier. In each sample, clear peaks are visible that correspond to reflections (001), (002) and (003).

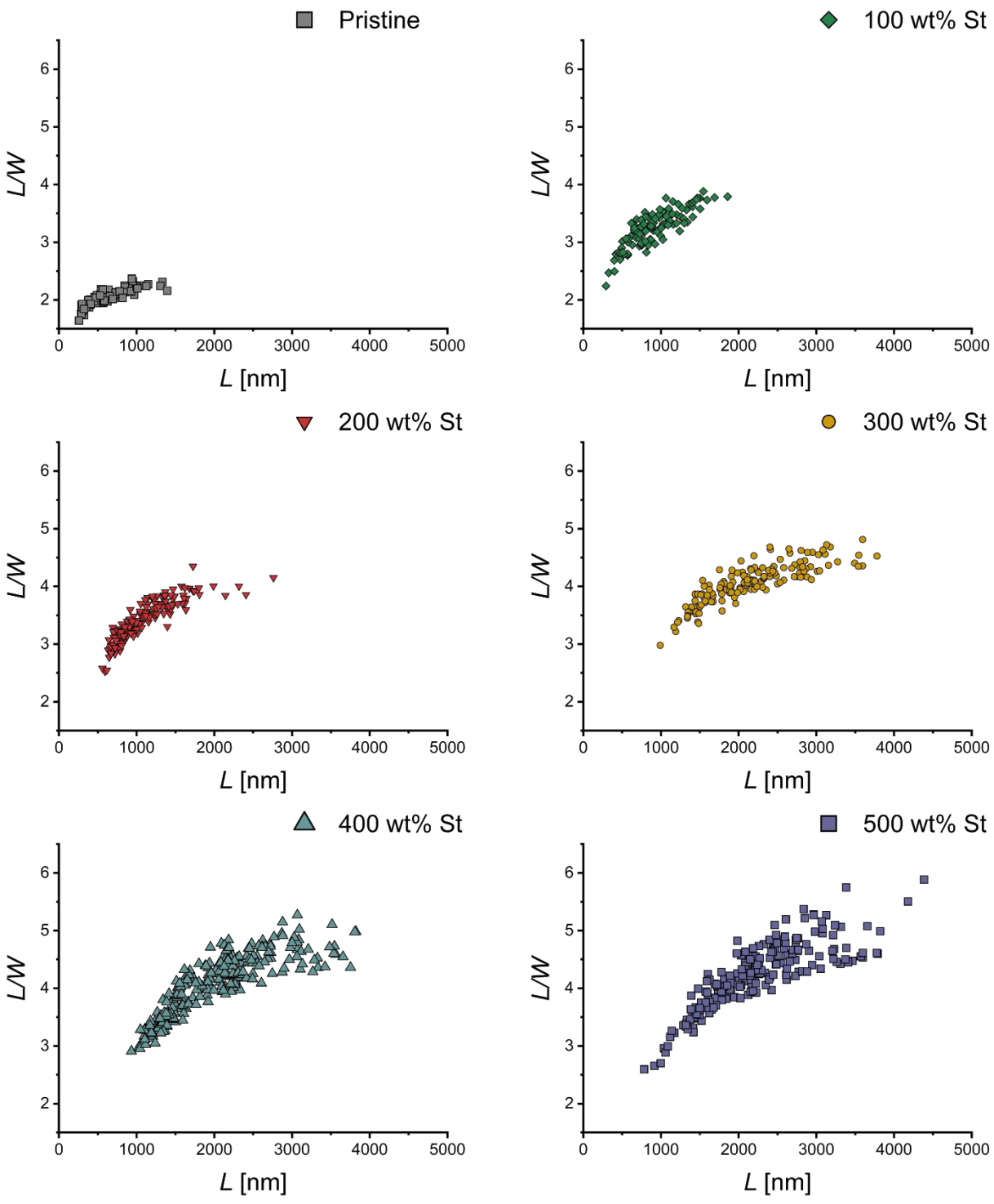

Figure S13. Aspect ratio (AR = L/W) of crosslinked PS-*b*-P2VP particles (100 mol% of DBB) after seeded polymerization with different amounts of styrene. Each graph depicts the dependence of *AR* on particle size (described by *L*).

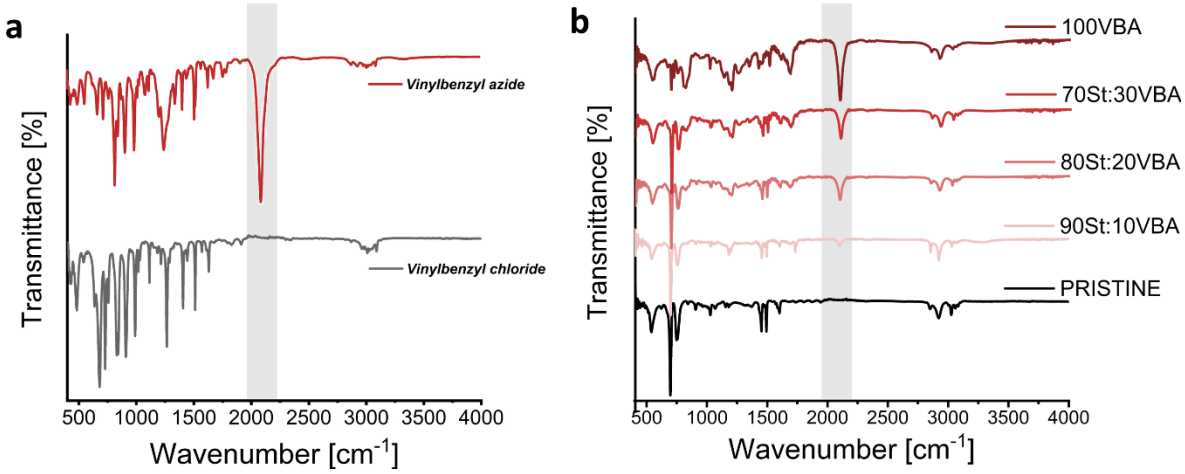

Figure S14. FTIR spectra of (a) the VBA monomer and (b) crosslinked particles (100 mol% DBB) after seeded copolymerization with different mixtures of St/VBA (400 wt% total monomer content). The highlighted band at 2189 cm^{-1} is assigned to the azide group from the reactive VBA units.

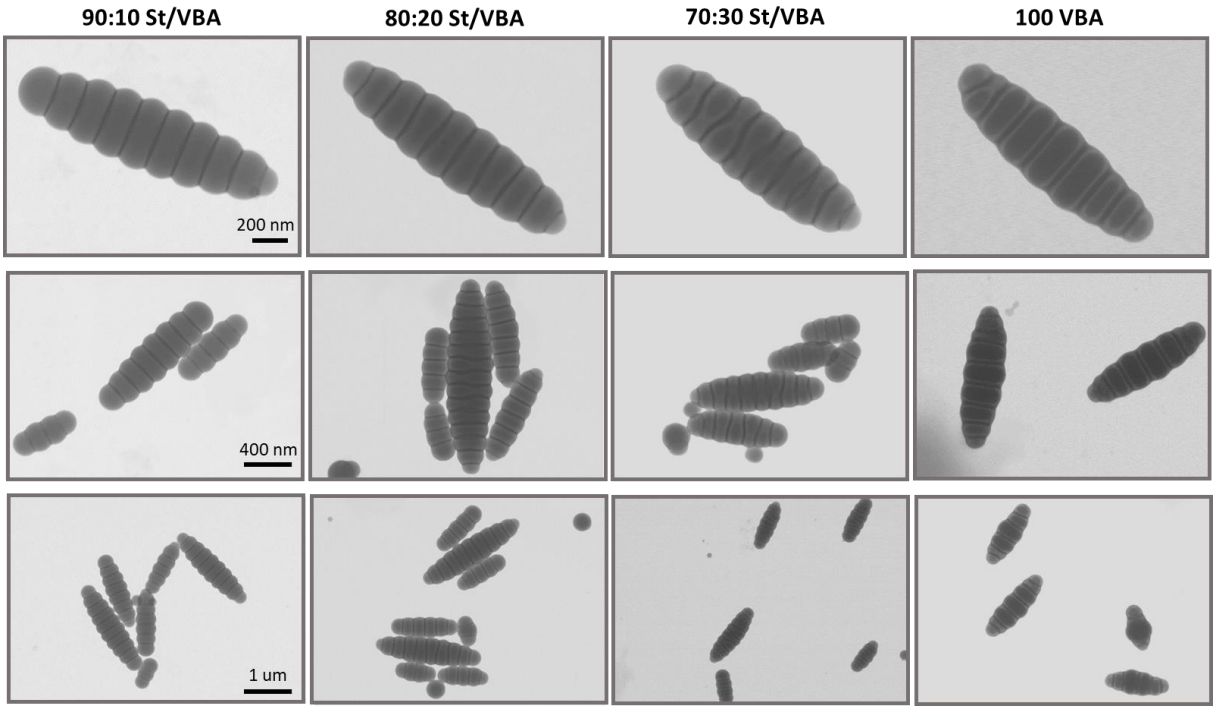

Figure S15. TEM images of crosslinked particles (100 mol% DBB) after seeded copolymerization with different mixtures of St/VBA (400 wt% total monomer content). Azide groups give a dark contrast due to the interaction with the iodine during staining.

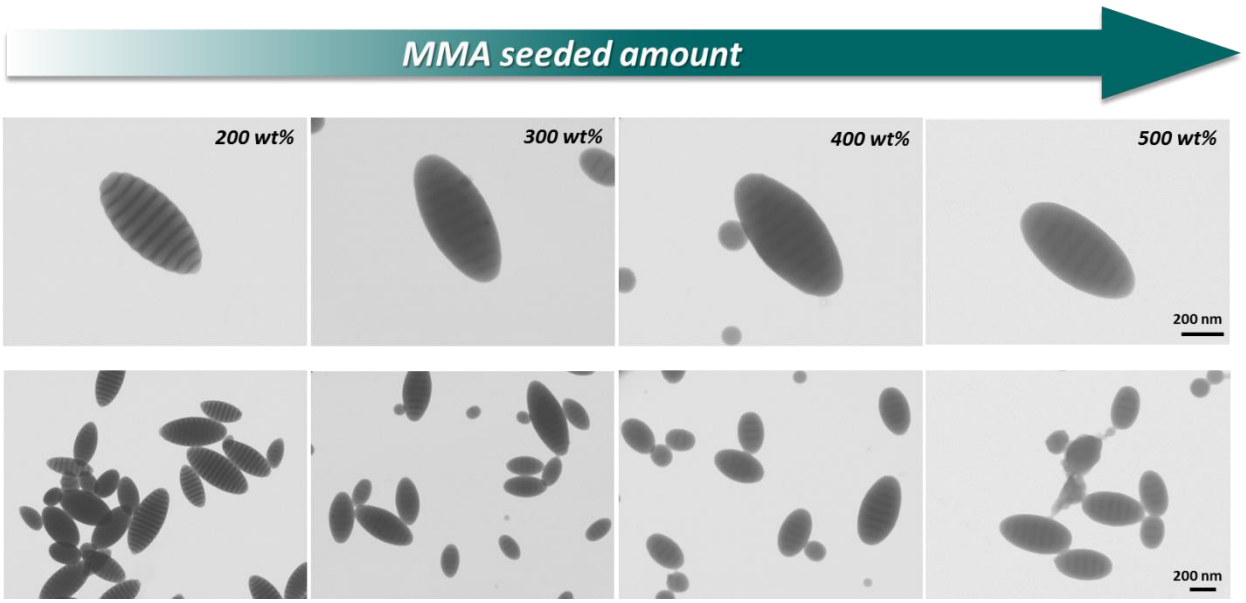

Figure S16. TEM images of PS-*b*-P2VP particles after seeded polymerization with methyl methacrylate (MMA) as monomer. The upper part shows detailed pictures of single particles for each MMA content. The lower part shows the same samples with lower magnification. The use of a neutral monomer that has no affinity for either domain generates a phase separation and migration of the PMMA to the particle surface.

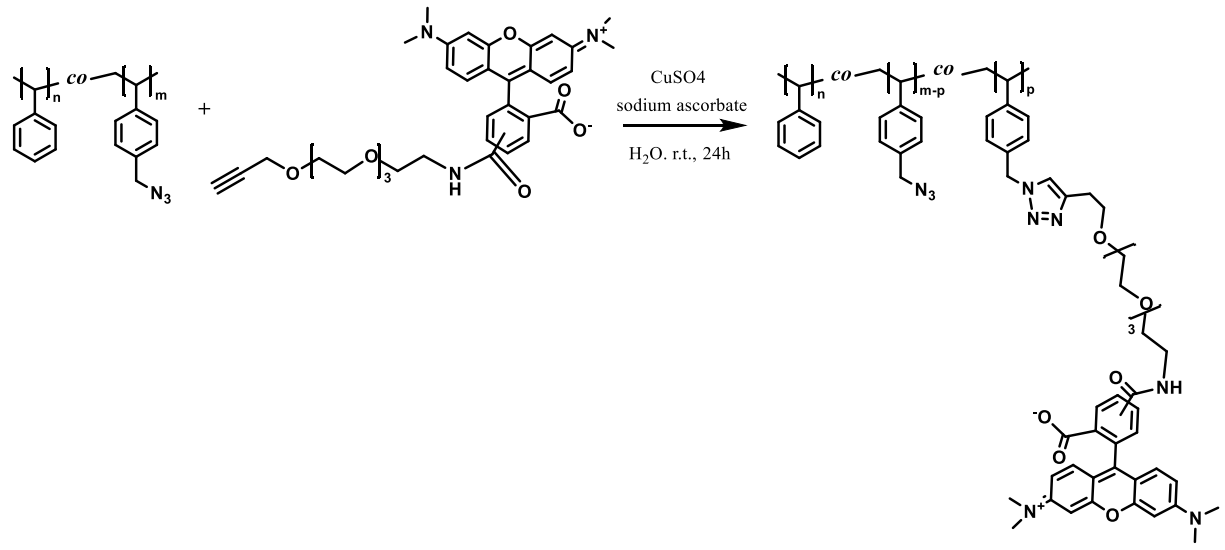

Scheme S1. CuAAC click functionalization of reactive PS/PS-*co*-PVBA domains with TAMRA-alkyne dye.

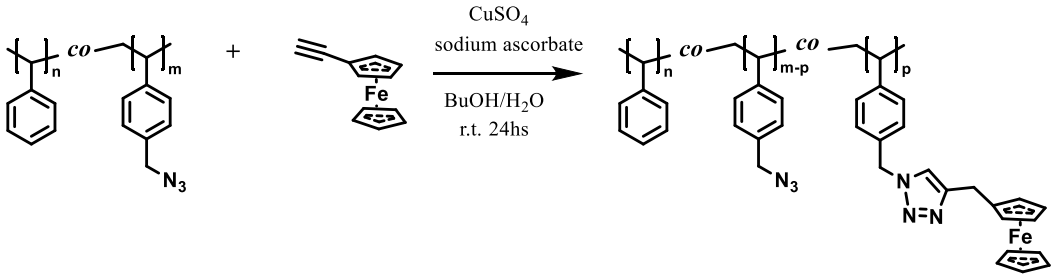

Scheme S2. CuAAC click functionalization of reactive PS/PS-*co*-PVBA domains with FCN-alkyne.

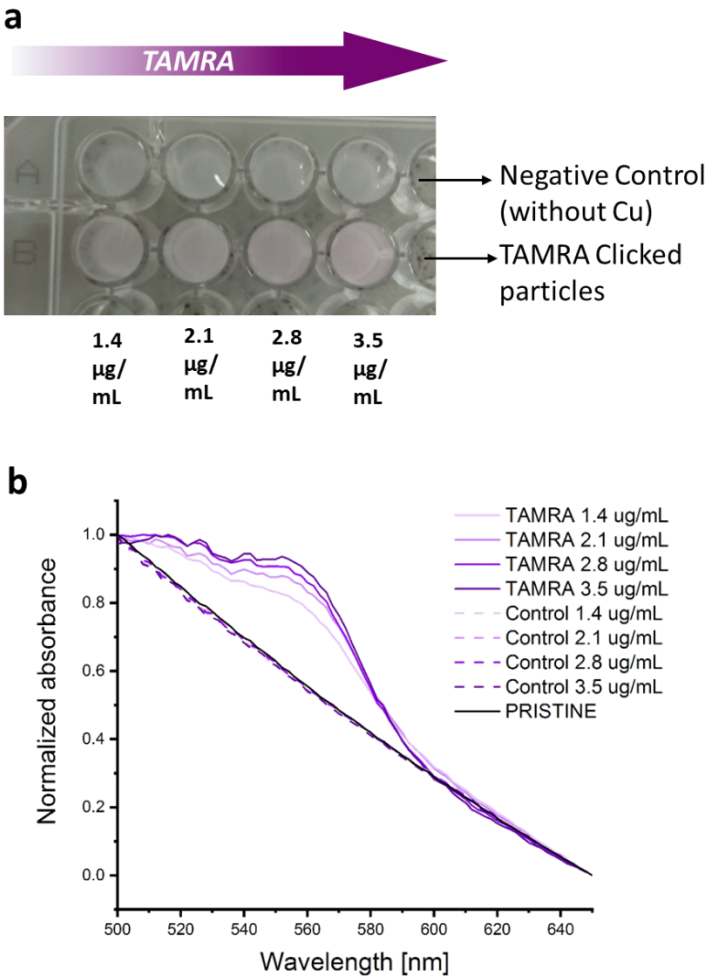

Figure S17. CuAAC click functionalization of reactive particles (90:10 St:VBA, total 400 wt%) using TAMRA-alkyne. a) Optical image of a well-plate containing the functionalized particles after 4 cycles of washing. The upper row contains the negative control samples, i.e., addition of the same amount of TAMRA-alkyne but without Cu. Non-colored dispersions suggest that physical entrapment/adsorption of dye in/on the particle is negligible. The bottom row depicts the samples after CuAAC click reaction. All samples show a purple color that increases in intensity with concentration of TAMRA-alkyne used during the click reaction. b) Intensity-normalized FTIR spectra of the negative controls, TAMRA-clicked particles, and pristine particles.

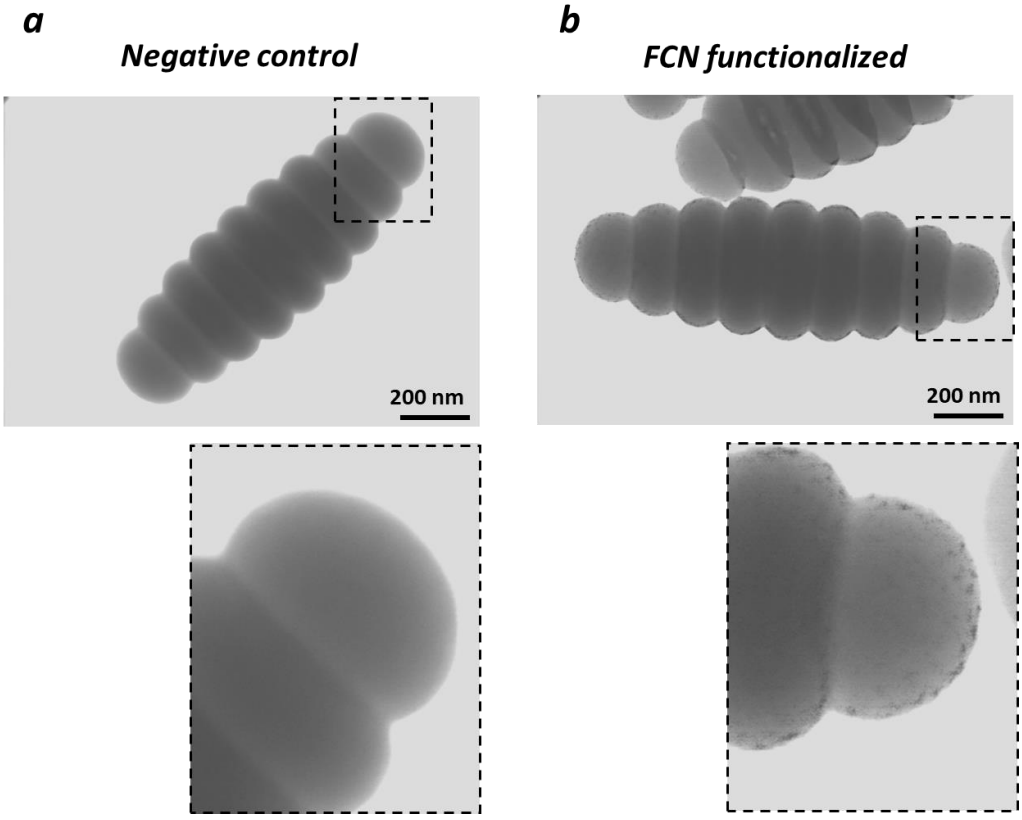

Figure S18. CuAAC click functionalization of reactive particles (90:10 St:VBA, total 400 wt%) using FCN-alkyne. a) TEM picture of negative control sample, i.e., addition of the same amount of 1eq of FCN-alkyne but without Cu. b) TEM picture of a functionalized FCN sample. Fe from the FCN can be visualized in unstained particles due to the good Z-contrast.

REFERENCES

[1] a) D. Klinger, C. X. Wang, L. A. Connal, D. J. Audus, S. G. Jang, S. Kraemer, K. L. Killops, G. H. Fredrickson, E. J. Kramer, C. J. Hawker, *Angew. Chem. Int. Ed.* **2014**, *53*, 7018-7022; b) B. V. K. J. Schmidt, C. X. Wang, S. Kraemer, L. A. Connal, D. Klinger, *Polym. Chem.* **2018**, *9*, 1638-1649.

[2] a) J. Filik, A. W. Ashton, P. C. Y. Chang, P. A. Chater, S. J. Day, M. Drakopoulos, M. W. Gerring, M. L. Hart, O. V. Magdysyuk, S. Michalik, A. Smith, C. C. Tang, N. J. Terrill, M. T. Wharmby, H. Wilhelm, *Journal of Applied Crystallography* **2017**, *50*, 959-966; b) B. R. Pauw, A. J. Smith, T. Snow, N. J. Terrill, A. F. Thünemann, *Journal of Applied Crystallography* **2017**, *50*, 1800-1811.

[3] S. Lee, J. J. Shin, K. H. Ku, Y. J. Lee, S. G. Jang, H. Yun, B. J. Kim, *Macromolecules* **2020**, *53*, 7198-7206.